Gravity Wave Radiation and Mean Responses to Local Body Forces in the Atmosphere

SHARON L. VADAS AND DAVID C. FRITTS

Colorado Research Associates Division, NorthWest Research Associates, Inc., Boulder, Colorado

(Manuscript received 4 May 2000, in final form 11 December 2000)

ABSTRACT

The authors determine the spectral linear solutions that arise in response to local 3D body forces and heatings in an idealized environment that turn on and off smoothly but not necessarily slowly over a finite interval in time. The solutions include impulsive through slowly varying body forcings. The forcings result in both a mean response, which is typically significantly broadened spatially in one direction, and a gravity wave response, which allows the fluid to reach this state. The gravity wave field depends on both the spatial attributes of the source and the forcing duration. The frequency of the wave response is the ''characteristic'' source frequency (formed from the source dimensions) if the forcing frequency is greater than the characteristic frequency and is the forcing frequency otherwise. The radiated gravity waves from zonal forcings have vertical wavelengths, which are approximately twice the vertical extent of the forcing, and horizontal wavelengths, which are at least twice the horizontal extent of the forcing. Wave excitation is increasingly inefficient when the forcing frequency is smaller than the characteristic source frequency. In addition, the mean responses are not confined to the source region; in general, significant spatial broadening of the mean responses occurs. If the source's frequency is high and low, the responses are broadened horizontally and vertically, respectively, with the amount depending on the characteristic scales of the source. If the body forcing is in the eastward direction, then much or all of the ensuing zonal mean wind is eastward. However, for many realistic forcing scenarios, a large percentage of the ensuing zonal wind flows westward. These countersigned jets are displaced meridionally about the source. Thus, spatially confined body forcings create both gravity wave and mean responses if the forcings are fast enough; very slowly varying forcings create only mean responses.

1. Introduction

Body forcing due to gravity wave dissipation and momentum flux divergence is now understood to contribute to mean atmospheric structures at many altitudes. Orographic gravity wave flux divergence contributes to systematic zonal wind reductions and tropospheric jet closure in the summer lower stratosphere, where dissipation is enhanced by light winds and high stability (Palmer et al. 1986; McFarlane 1987; VanZandt and Fritts 1989). In the middle and upper stratosphere, flux divergence accompanying nonstationary gravity waves appears to play an accelerative role at lower and middle latitudes (Alexander and Rosenlof 1996; Alexander 1997) and to contribute to a separated polar winter stratopause (Hitchman et al. 1989). Gravity wave flux divergence appears to have its largest (known) influences, however, in the mesosphere and lower thermosphere, where it causes zonal torques of $\sim$100 m s^{-1} day^{-1}, closure of the mesospheric jets, an induced residual circulation from the summer to winter hemisphere, and a corresponding reversal of the mean meridional temperature gradient near the mesopause (Nastrom et al. 1982; Holton 1982, 1983; Dunkerton 1982; Garcia 1987). Indeed, localized gravity wave forcing appears to account for many of the unique characteristics of the summer mesopause region (McIntyre 1989; Garcia 1989; Fritts and Luo 1995; Luo et al. 1995). The general principles have been addressed theoretically (McIntyre 1989; Dunkerton 1989), leading to the concept of ''downward control'' of the meridional circulation by wave Eliassen–Palm (EP) flux divergence applied at greater altitudes (Haynes et al. 1991; Garcia and Boville 1994).

Despite our current qualitative understanding of gravity wave forcing in the lower and middle atmosphere, we know virtually nothing of its role at thermospheric altitudes. Nevertheless, we might expect that the possible effects may be large because of the significant mean fluxes at lower thermospheric altitudes, the propagation and filtering characteristics of gravity waves, and the implications of ''downward control'' at these altitudes. Indeed, there is some evidence that gravity waves generated by convection and orography propagate to very high altitudes (Taylor and Hapgood 1988; Kelley 1997). Other processes also induce local body forces at various altitudes. Tropospheric convection contributes heat and vertical momentum sources, and unbalanced flows undergo adjustment, while Joule heating,

Corresponding author address: Dr. Sharon L. Vadas, Colorado Research Associates Division, NorthWest Research Associates, Inc., 3380 Mitchell Lane, Boulder, CO 80301.
E-mail: sharon.vadas@colorado-research.com

auroral precipitation, and ion drag are significant sources at higher altitudes.

At present, we have an incomplete understanding of the role of spatial and temporal variability of gravity wave flux divergence in radiating additional gravity waves. Studies have been performed with localized two- or three-dimensional (2D or 3D) initial conditions and body forcings; however, the momentum was assumed to be deposited either impulsely in time (i.e., instantaneously at $t = 0$) or as a step function in time (i.e., turns on instantaneously at $t = 0$ and turns off instantaneously at $t = \sigma$) (Dickinson 1969; Blumen 1972; Walterscheid and Boucher 1984; Zhu and Holton 1987; Fritts and Luo 1992; Luo and Fritts 1993; Bühler et al. 1999). While illustrative and useful in describing the mean and oscillatory responses for certain types of body forcings, these studies do not describe the general responses to realistic atmospheric body forcings. For example, a recent 2D simulation shows that when waves generated by tropospheric convection break in the mesosphere, zonal momentum is deposited with a complicated temporal evolution, which includes both low- and high-frequency temporal components (Holton and Alexander 1999). In addition, Holton and Alexander (1999) and Satomura and Sato (1999) find that secondary waves are generated and radiate away from simulated wave-breaking regions, which may be due in part to the momentum deposition process described herein. Toward this end, we investigate in this paper body forcings that evolve as $\sin^2(\ldots t)$ over a finite interval, so that a linear superposition of these solutions can approximate a complicated, temporally evolving body forcing. Because the forcing turns on and off smoothly, it more realistically mimics an atmospheric wave-dissipation event and eliminates any unrealistic oscillatory responses that result from the instantaneous turn on and off of the step function forcings. Sensitivity studies with differing forcing frequencies result in a quantitative understanding of the amplitudes and wavelengths of the radiated gravity waves from differing temporal frequency components. Therefore, the present work illuminates the adjustment process accompanying local body forcing in the atmosphere more realistically and in more detail than previously described.

We are interested here in describing the characteristics of radiated gravity waves and mean responses to general body forcings (e.g., wave breaking, ion drag, unbalanced flows undergoing adjustment, etc.). Perhaps the most important body forcing in the middle atmosphere is due to wave breaking. We parameterize the deposition of momentum from a wave-dissipation event as a body forcing with spatial and temporal scales imposed by the source, filtering, and interaction processes that control gravity wave momentum transport with altitude. This involves an assessment of both the characteristic wave scales or frequencies and the extent and structure of the response in space and time. In the case of orography, isolated convection, or frontal systems, typical wave scales and frequencies are about tens to hundreds of kilometers and tens of minutes to hours, while a wave packet extent may increase from about tens of kilometers near the source to hundreds of kilometers at stratospheric altitudes (Durran and Klemp 1987; Gall et al. 1988; Nastrom and Fritts 1992; Fritts and Nastrom 1992; Fovell et al. 1992; Alexander et al. 1995; Alexander 1996). High-frequency waves account for a large part of momentum transport (and the higher-frequency variability of the body forcing) at greater altitudes, while characteristic frequencies do not vary much, though the spatial scales likely increase with altitude (Fritts and VanZandt 1993). Influences of filtering and wave–wave interaction processes at higher altitudes are more difficult to guess. Nevertheless, time series of velocity and temperature data typically show that wave trains last for ~3 to 10 cycles, suggesting that body forces extend about hundreds of kilometers here as well. Timescales for such forcing may also be imposed by filtering conditions accompanying the larger-amplitude tidal features (Fritts and Vincent 1987), which contribute to variable momentum fluxes that may be much larger than mean values. In this case, typical depth scales of the forcing are ~10 to 20 km, with corresponding timescales of a few hours. Forcing by lower-frequency gravity waves also surely occurs, but this forcing is clearly distributed over larger spatial domains, occupies longer intervals of time, and almost certainly involves much smaller body forces due to the smaller vertical group and perturbation velocities of such motions.

In order to characterize the duration of the body forcing, we note that the forcing cannot occur on timescales too much shorter than the characteristic period of the wave field (which controls the rate of vertical momentum flux and the timescale for wave dissipation). And it is not likely to occur on timescales much less than the duration of the wave packet as a whole. Thus, given that typical wave packets exhibit a few to a few tens of oscillations in middle atmosphere measurements and that the intrinsic wave periods accounting for the majority of gravity wave momentum flux are about an hour or less, we assume that typical forcing intervals occupy ~1 to 10 h.

Although we are primarily interested in describing the scales, frequencies, and amplitudes of gravity waves radiated from atmospheric body forcings, we will also investigate the mean responses to these body forcings, as they are obtained ''for free'' in our spectral solutions. These mean responses are due solely to the effects of the body forcing and occur whether or not gravity waves are excited from the forcing. Because our solutions are derived from the linear equations, wave-mean interactions and other nonlinear effects will not be considered here. Our goal in this paper is to use analytic techniques to explore the ramifications of body forces on the mean and radiated gravity wave responses due to gravity wave momentum flux divergence that are localized both spatially and temporally. Our primary motivations include 1) the considerable variability of gravity wave momentum fluxes in

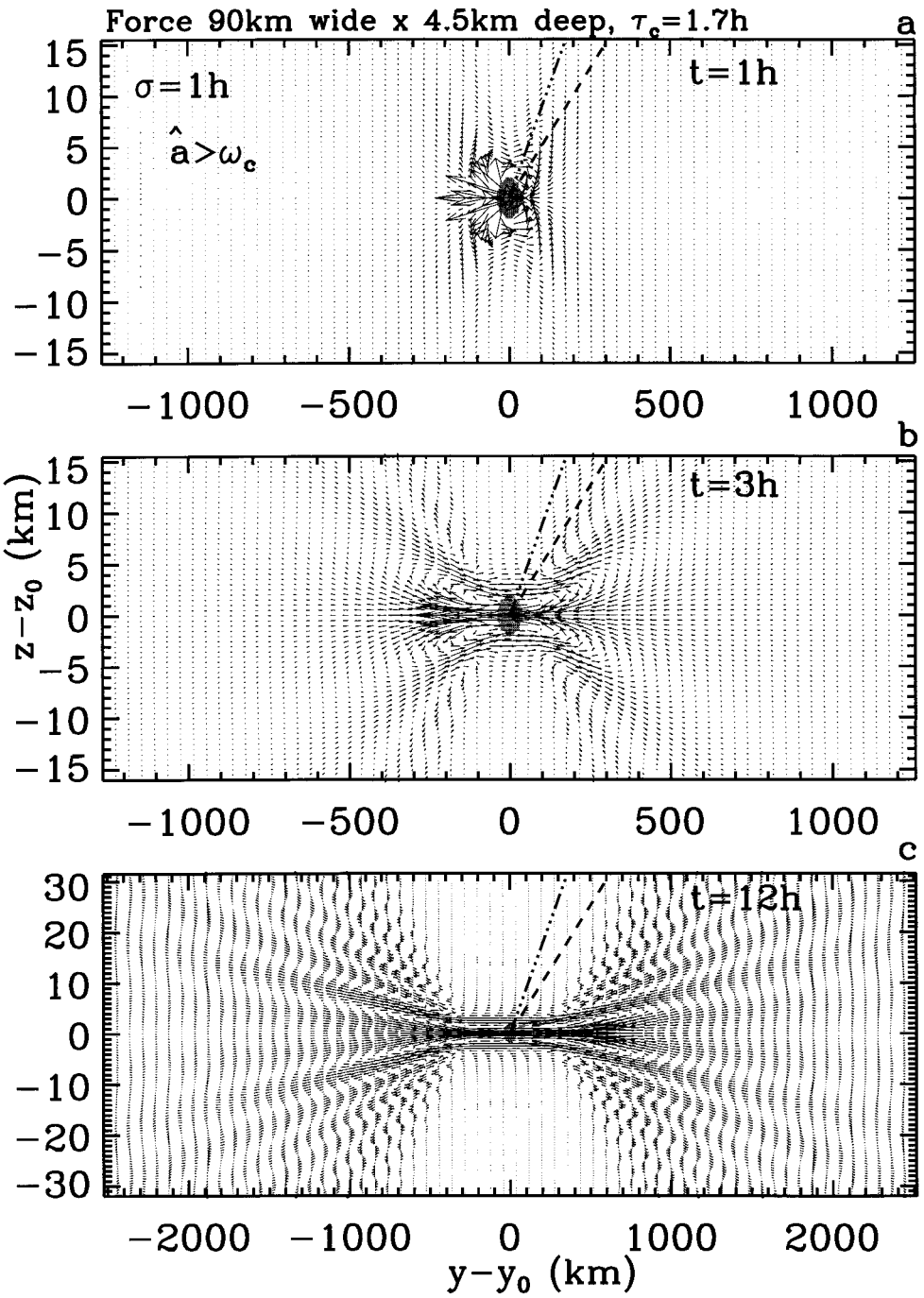

FIG. 1. Gravity wave plus mean responses that result from a longitudinally symmetric monopole zonal body forcing with $\sigma_y = 20$ km, $\sigma_z = 1$ km, $n = 1$, and $\sigma = 1$ h. For this source, $\tau_c = 1.7$ h so that $\hat{a} > \omega_c$. The velocity vectors at $t = 1$, 3, and 12 h are shown in (a), (b), and (c), respectively. The body forcing region is shaded at the >10% level. The domain is increased in (c). The dash lines indicate the angles $\sin^{-1}(\omega_c/N) = 2.9°$ from the source center, while the dash-dot-dot-dot lines indicate the angles $\sin^{-1}(\hat{a}/N) = 5.0°$ from the source center. For this illustration, $N_y = 1024$, $N_z = 256$. This figure does not depend on the forcing amplitude as long as the linear approximation is satisfied (true for all illustrations). This is because both u and w scale as u_0.

TABLE 1. Symbols and notation.

$F_x(\mathbf{x})$, $F_y(\mathbf{x})$, $F_z(\mathbf{x})$	Body force in x, y, and z directions, respectively
J	Heat source
F_ζ	External (vertical) vorticity forcing $\partial F_y/\partial x - \partial F_x/\partial y$
F_δ	External divergence forcing $\partial F_x/\partial x + \partial F_y/\partial y + \partial F_z/\partial z$
$\tilde{u}$, $\tilde{F}_x$, . . .	Fourier transform of u, F_x $(\mathbf{x})$, . . .
$\overline{u}$, $\overline{\tilde{u}}$, $\overline{E}$, . . .	Mean (averaged in time) u, $\tilde{u}$, E, . . .
$\mathcal{F}(t)$	Temporal evolution of forcing (i.e., body force and heating)
σ	Total forcing duration
$\hat{a}$	Forcing frequency $2\pi n/\sigma$
n	Number of cycles in forcing
u_0	Amplitude of zonal forcing
σ_x, σ_y, σ_z	Half-widths of the source in x, y, and z, respectively
k_c, l_c, m_c	Characteristic wavenumbers of the source, $k_c = \sigma_x^{-1}$, etc.
κ	Characteristic horizontal wavenumber, $k_{Hc} = \sqrt{k_c^2 + l_c^2}$
R	Rossby deformation radius $\sigma_z N/f$
ω_c	Characteristic source frequency, $\omega_c = f\{[1 + (\kappa R)^2]/[1 + (\sigma_z\kappa)^2]\}^{1/2}$
$\mathcal{S}$	$\sin\omega t + \sin\omega(\sigma - t)$
$\mathcal{C}$	$\cos\omega t - \cos\omega(\sigma - t)$
Δ_x, Δ_y, Δ_z	Half-widths of broadened mean responses in x, y, and z, respectively

space and time, 2) the likely importance of the variable component(s) of this forcing in both mean forcing and additional gravity wave excitation at larger scales of motion, and 3) the potential that these larger-scale radiated gravity waves may propagate to much greater altitudes and contribute to presently unknown effects because of their larger scales and phase speeds.

We organize this paper as follows. We obtain formal solutions describing the linear response to local, time-dependent body forces and heatings in an unsheared environment with constant buoyancy frequency in sections 2 and 3. Section 4 shows the radiated gravity wave spectra for various longitudinally symmetric body forcings. Section 5 illustrates some post forcing mean responses to 2D and 3D body forces. Section 6 contains a summary and discussion of our results.

2. Equations and potential vorticity

a. Linear equations with local body forcing

We consider a 3D, local body forcing of the atmosphere, which is created by gravity wave dissipation processes, ion drag, adjustment to unbalanced flows, etc. The dissipation process gives rise to a vertical wave momentum flux divergence or EP flux divergence, which acts on the fluid as a zonal body force (Andrews et al. 1987). Meridional and vertical body forcing can also occur for waves generated, for example, from convective systems, mountains having nonlongitudinal alignments, or for waves that are filtered by lower-frequency or mean motions. Heat may be deposited through wave dissipation or another process and will also be considered as a source term in our derivation. We assume that the forcing amplitudes are small (so that wave–mean flow and wave–wave interactions can be neglected), that the vertical extent of this force is smaller than a density scale height (assumed to be $H \simeq 7$ km), and that the Mach number is less than one. We also assume that the background atmosphere is isothermal and unsheared and that it is inviscid, since the scales of the forcing, wave responses, and mean responses we are considering are much larger than the scale at which diffusion is operative. Our goal is to provide simple and insightful solutions to aid in understanding the *generation* of the mean and gravity wave responses in an idealized background but not the propagation and/or dissipation of these responses. (Hereafter, ''radiated gravity waves'' or ''gravity wave responses'' refer to the gravity waves created by the body forcing). The 3D linear,[1] Boussinesq, incompressible, f-plane equations that describe this situation are

$$\frac{\partial u}{\partial t} + \frac{1}{\overline{\rho}}\frac{\partial p'}{\partial x} - fv = F_x(\mathbf{x})\mathcal{F}(t), \tag{2.1}$$

$$\frac{\partial v}{\partial t} + \frac{1}{\overline{\rho}}\frac{\partial p'}{\partial y} + fu = F_y(\mathbf{x})\mathcal{F}(t), \tag{2.2}$$

$$\frac{\partial w}{\partial t} + \frac{1}{\overline{\rho}}\frac{\partial p'}{\partial z} - \frac{g}{\overline{\theta}}\theta' = F_z(\mathbf{x})\mathcal{F}(t), \tag{2.3}$$

$$\frac{\partial \theta'}{\partial t} + \frac{\overline{\theta}N^2}{g}w = \frac{\overline{\theta}}{g}J(\mathbf{x})\mathcal{F}(t), \tag{2.4}$$

$$\frac{\partial u}{\partial x} + \frac{\partial v}{\partial y} + \frac{\partial w}{\partial z} = 0, \tag{2.5}$$

where N is the buoyancy frequency; u, v, and w are the zonal, meridional, and vertical velocities, respectively; θ' is the perturbation potential temperature; p' is the perturbation pressure; the overlines denote the mean values; and $\overline{\theta}$ and $\overline{\rho}$ are the constant background potential temperature and density, respectively. We illustrate our solutions with upper mesosphere, midlatitude values of $N = 2 \times 10^{-2}$ s^{-1}, $f = 1 \times 10^{-4}$ s^{-1}, $\overline{\theta} = 10\,241$ K, and $g = 9.53$ m s^{-2}, although our theory is applicable throughout the atmosphere. The ''interval'' body forcing/heating has frequency $\hat{a}$, temporal evolution $\mathcal{F}(t) \propto \sin^2(\hat{a}t/2)$ for $t = [0, \sigma]$, and $\mathcal{F} = 0$ for $t \geq \sigma$. Both $\mathcal{F}$ and $d\mathcal{F}/dt$ are continuous for $t \geq 0$. Additionally, the spatial distributions are $F_x(\mathbf{x})$, $F_y(\mathbf{x})$, $F_z(\mathbf{x})$, and $J(\mathbf{x})$ (hereafter called ''sources''). Table 1 shows some important symbols used in this paper.

Where rotation is important, the response of the fluid

[1] Appendix A contains crude estimates as to how small a zonal body forcing must be in order to neglect the nonlinear wave–wave and wave-mean terms. Vadas et al. 2001, (unpublished manuscript) contains a better estimate as to when these nonlinear terms can be neglected. It is found that nonlinear terms are generally only important when compressible effects are important as well.

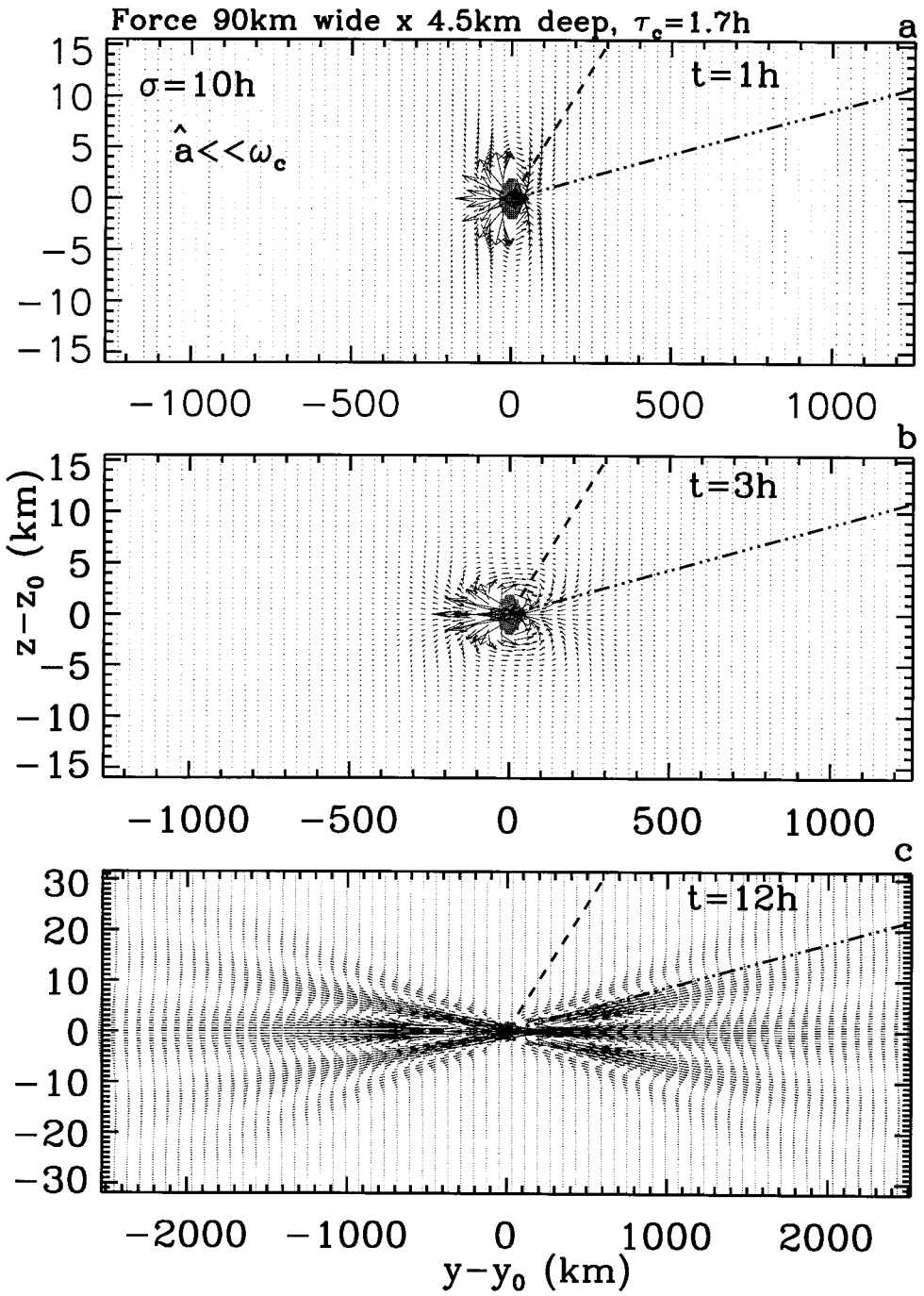

FIG. 2. Same as in Fig. 1 but for the much longer forcing duration of σ = 10 h. Here, $\hat{a} \ll \omega_c$. The dash lines indicate the angles $\sin^{-1}(\omega_c/N) = 2.9°$, while the dash-dot-dot-dot lines indicate the angles $\sin^{-1}(\hat{a}/N) = 0.5°$.

TABLE 2. Temporal variability used to generate solid lines in Fig. 7.

μ_0 (m s^{-1})	0.05	0.13	0.05	0.03	0.14	0.20	0.20	0.10	0.07	0.03
σ (h)	10.0	5.0	7.0	8.0	7.0	9.0	10.0	10.0	10.0	10.0
n	1	1	4	2	3	3	5	10	12	20
t_0 (h)	0.0	0.5	1.0	1.0	1.0	0.5	0.0	0.0	0.0	0.0
σ/n (min)	600.0	300.0	105.0	240.0	140.0	180.0	120.0	60.0	50.0	30.0

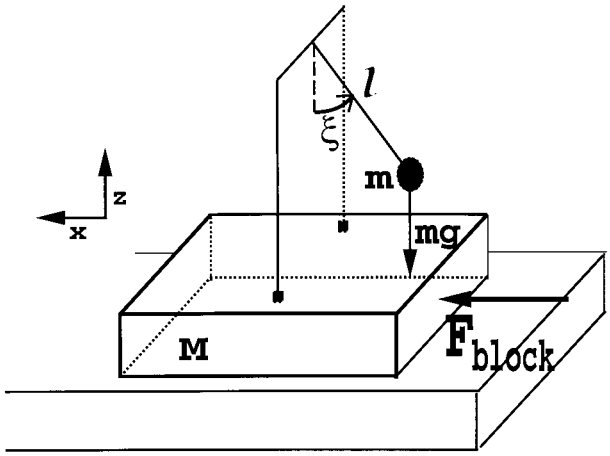

FIG. 3. The Newtonian ball-and-block setup.

to a body force is the geostrophic adjustment process, first studied by Rossby (1936, 1937, 1938), whereby a balanced mean state is attained through the radiation of nongeostrophic gravity waves. This process has been studied from initial conditions, impulsive forcing, and temporal step function forcing (Dickinson 1969; Blumen 1972; Zhu and Holton 1987; Fritts and Luo 1992; Luo and Fritts 1993; Bühler et al. 1999). Since $\mathcal{F}(t)$ turns on and off in a smooth manner for the forcings in this paper, the solutions derived herein are likely more realistic than the solutions obtained by Zhu and Holton (1987) (which were derived with a temporal step function body forcing) because our solutions do not contain an excess of gravity waves that result from the discontinuous turn on and off of the body forcing (see section 3e). In addition, the solutions derived here will describe the characteristic frequencies and scales of radiated gravity waves better than those from the impulsive solutions by Fritts and Luo (1992) and Luo and Fritts (1993) due to the temporal variability present in real middle atmosphere wave-dissipation processes. Finally, the solutions derived herein generalize previous solutions in that they contain the gravity wave and mean responses from vertical and horizontal body forcings as well as from heatings.

b. Induced potential vorticity

The potential vorticity is conserved in geostrophic adjustment processes for which initial conditions are specified (Gill 1982). Zhu and Holton (1987) generalized this concept to include external divergence and vorticity forcings. Following them, Eqs. (2.1)–(2.5) become

$$\frac{\partial \zeta_\theta}{\partial t} = \left(F_\zeta + \frac{f}{N^2}\frac{\partial J}{\partial z}\right)\mathcal{F}, \tag{2.6}$$

where $F_\zeta = \partial F_y/\partial x - \partial F_x/\partial y$ is the external (vertical) vorticity forcing,

$$\zeta_\theta = \zeta + \frac{f}{N^2}\frac{g}{\bar{\theta}}\frac{\partial \theta'}{\partial z} \tag{2.7}$$

is the induced potential vorticity,[2] and $\zeta = \partial v/\partial x - \partial u/\partial y$ is the fluid vorticity. In the absence of forcing and dissipation, the potential vorticity is conserved in time. The time integration of the vorticity forcing and heating gives the steady geostrophic mode. Using Eq. (2.6), the induced potential vorticity at time t is

$$\zeta_\theta(t) = \zeta_\theta(0) + \left(F_\zeta + \frac{f}{N^2}\frac{\partial J}{\partial z}\right)\int_0^t \mathcal{F}(t')\,dt'. \tag{2.8}$$

For "equal-momentum forcings" (which we define here to be forcings for which $\int_0^\sigma \mathcal{F}(t')\,dt' = 1$, where $\mathcal{F}(t) = 0$ for $t \geq \sigma$) and for a given spatial source, the postforcing (i.e., $t \geq \sigma$) induced potential vorticity does not depend on the details of the temporal variability contained in the function $\mathcal{F}(t)$; the shape, amplitudes, and interval length of $\mathcal{F}(t)$ do not influence the postforcing steady mean response. For a given source then, the step function in time forcing (see section 3e) and the $\sin^2(\ldots t)$ forcing with any duration length [see Eq. (3.5); includes an impulsive forcing] both create the same postforcing mean response.

3. Interval body forcing solution

a. Solution methods

We expand u, v, w, p', θ', F_x, F_y, F_z, and J in a Fourier series,[3] for example,

$$u(x, y, z, t) = \frac{1}{(2\pi)^3}\iiint e^{-ikx-ily-imz}\tilde{u}(k, l, m, t)\,dk\,dl\,dm, \tag{3.1}$$

[2] Defining $\phi = p'/\bar{\rho}$, setting $F_z = J = 0$, $H \to \infty$, and neglecting the vertical acceleration, we recover Eq. (24) in Zhu and Holton (1987), $\zeta_\theta = \zeta + f\phi_{zz}/N^2$.

[3] All integrals not explicitly marked are evaluated from $-\infty$ to ∞.

TABLE 3. Spatial broadening of postforcing mean responses from zonal forces.

$\sqrt{\mathbf{k}_c^2\omega_c^2} \simeq$ broadens in	Monopole			Dipole-in-x			Dipole-in-y			Dipole-in-z		
	$m_c f$ z	$l_c N$ y	$k_c N$ x	$m_c f$ z	$l_c N$ y	$k_c N$ x	$m_c f$ z	$l_c N$ y	$k_c N$ x	$m_c f$ z	$l_c N$ y	$k_c N$ x
u	√	—	√	√	—	√	√	—	√	√	—	√
v	√	√	√	√	√	—	√	—	√	√	√	√
θ'	√	√	√	√	√	√	√	—	√	—	√	√

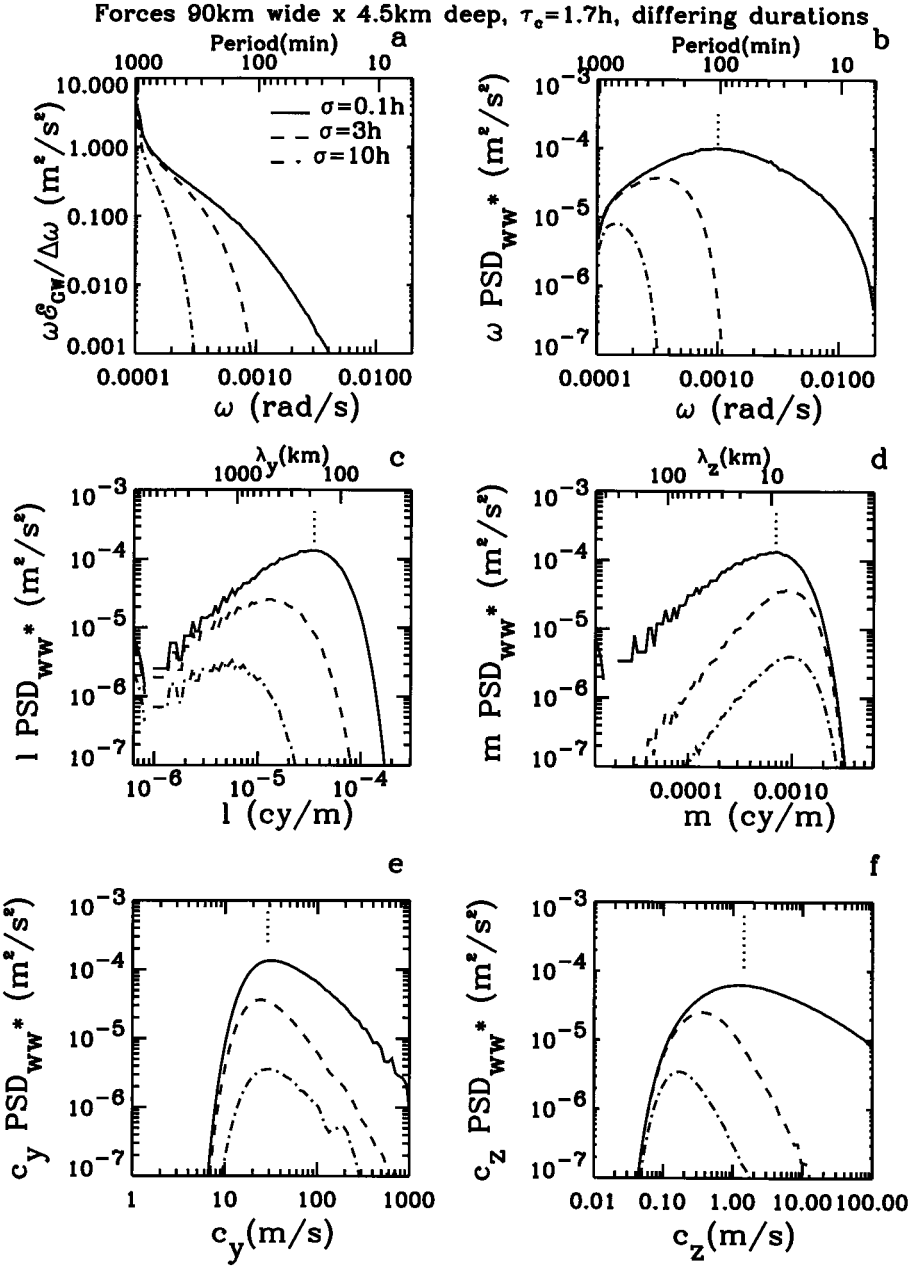

FIG. 4. Gravity wave spectra in variance content form from longitudinally symmetric monopole zonal body forcings with σ_y = 20 km, σ_z = 1 km, n = 1, and u_0 = 1 m s^{-1}. The solid, dash, and dash-dot lines are for σ = 0.1 h, σ = 3 h, and σ = 10 h, respectively. The dotted lines in (b)–(f) are located at $\omega = \omega_c$, $\lambda_y = 9\sigma_y$, $\lambda_z = 9\sigma_z$, $c_y = \omega_c 9\sigma_y/2\pi$, and $c_z = \omega_c 9\sigma_z/2\pi$, respectively. The solid lines are the spectra for essentially impulsive forcings. For these illustrations, $t = \sigma$ and $N_y = N_z = 1024$.

where "~" denotes the Fourier transform of the variable. We then take the Laplace transform of the equations (Abramowitz and Stegun 1972), then solve them algebraically. The Laplace transform of $\tilde{w}(t)$, denoted $\mathcal{L}_{\tilde{w}(t)}$, is

$$\mathcal{L}_{\tilde{w}(t)} = \frac{A_I s + B_I}{s^2 + \omega^2} + \frac{A_F s + B_F}{s^2 + \omega^2}\mathcal{L}_{\mathcal{F}} \qquad (3.2)$$

where the Laplace transform of $\mathcal{F}(t)$ is $\mathcal{L}_{\mathcal{F}}$, the total wavenumber is $\mathbf{k} = (k, l, m)$, $\mathbf{k}^2 = k^2 + l^2 + m^2$, the horizontal wavenumber squared is $k_H^2 = k^2 + l^2$, and the wave frequency ω is

$$\omega^2 = \frac{(k_H^2 N^2 + m^2 f^2)}{\mathbf{k}^2}. \qquad (3.3)$$

The first term in Eq. (3.2) incorporates the initial condi-

tions [see Eq. (B6) and appendix B], while the last term incorporates the interval body forcing and heating with

$$A_{\rm F} = \tilde{F}_z - \frac{im\tilde{F}_\delta}{\mathbf{k}^2}, \qquad B_{\rm F} = \frac{k_H^2\tilde{J}}{\mathbf{k}^2} - \frac{imf\tilde{F}_\zeta}{\mathbf{k}^2}, \quad (3.4)$$

where $F_\delta = \partial F_x/\partial x + \partial F_y/\partial y + \partial F_z/\partial z$ is the external divergence forcing.

b. Spectral solutions

As discussed previously, $\mathcal{F}(t)$ turns on and off smoothly (but potentially quickly):

$$\mathcal{F}(t) = \frac{2}{\sigma}\begin{cases}\frac{1}{2}(1 - \cos\hat{a}t), & \text{for } 0 \le t \le \sigma,\\ 0, & \text{for } t \ge \sigma.\end{cases} \quad (3.5)$$

The function $\mathcal{F}$ is an equal-momentum forcing. The "forcing frequency" $\hat{a}$ is

$$\hat{a} \equiv 2\pi n/\sigma, \quad (3.6)$$

the "interval frequency" is $2\pi/\sigma$, and the number of forcing cycles is a positive integer, $n = 1, 2, 3, \ldots$. If $n = 1$, then the interval length σ equals the forcing period $2\pi/\hat{a}$. An impulsive forcing is a special case of this more general forcing and is obtained exactly by setting $n = 1$ and $\sigma = 0$ in Eq. (3.5). We take the inverse Laplace transform of Eq. (3.2) and solve.[4,5] Defining

$$D = \frac{1}{\sigma\omega^2(\hat{a}^2 - \omega^2)}, \quad (3.7)$$

the solution during the forcing (i.e., when $0 \le t \le \sigma$) for $\hat{a} \ne \omega$ is

$$\tilde{u}(t) = -\frac{il\tilde{F}_\zeta}{\sigma k_H^2}\left(t - \frac{\sin\hat{a}t}{\hat{a}}\right) - \frac{m}{\sigma\omega^2k_H^2}(lfB_{\rm F}t + lfA_{\rm F} + kB_{\rm F}) - \frac{Dm}{k_H^2}\left\{(lfA_{\rm F} + kB_{\rm F})(\omega^2\cos\hat{a}t - \hat{a}^2\cos\omega t) + \omega^2\left(\frac{lfB_{\rm F}}{\hat{a}} - k\hat{a}A_{\rm F}\right)\sin\hat{a}t + \hat{a}^2(k\omega A_{\rm F} - lfB_{\rm F}/\omega)\sin\omega t\right\}, \quad (3.8)$$

$$\tilde{v}(t) = \frac{ik\tilde{F}_\zeta}{\sigma k_H^2}\left(t - \frac{\sin\hat{a}t}{\hat{a}}\right) + \frac{m}{\sigma\omega^2k_H^2}(kfB_{\rm F}t + kfA_{\rm F} - lB_{\rm F}) + \frac{Dm}{k_H^2}\left\{(kfA_{\rm F} - lB_{\rm F})(\omega^2\cos\hat{a}t - \hat{a}^2\cos\omega t) + \omega^2\left(\frac{kfB_{\rm F}}{\hat{a}} + l\hat{a}A_{\rm F}\right)\sin\hat{a}t - \hat{a}^2(kfB_{\rm F}/\omega + l\omega A_{\rm F})\sin\omega t\right\}, \quad (3.9)$$

$$\tilde{w}(t) = \frac{B_{\rm F}}{\sigma\omega^2} + D\{A_{\rm F}\hat{a}\omega(\hat{a}\sin\omega t - \omega\sin\hat{a}t) + B_{\rm F}(\omega^2\cos\hat{a}t - \hat{a}^2\cos\omega t)\}, \quad (3.10)$$

$$\tilde{\Theta}(t) = \frac{\tilde{J}}{\sigma}\left(t - \frac{\sin\hat{a}t}{\hat{a}}\right) - \frac{N^2}{\sigma\omega^2}(B_{\rm F}t + A_{\rm F}) - N^2D\{A_{\rm F}(\omega^2\cos\hat{a}t - \hat{a}^2\cos\omega t) + B_{\rm F}(\omega^2\hat{a}^{-1}\sin\hat{a}t - \hat{a}^2\omega^{-1}\sin\omega t)\}, \quad (3.11)$$

$$\tilde{P}(t) = \frac{i}{m}\left[\frac{\tilde{J}}{\sigma}\left(t - \frac{\sin\hat{a}t}{\hat{a}}\right) - \frac{N^2}{\sigma\omega^2}(B_{\rm F}t + A_{\rm F})\right] - \frac{iD}{m}\{A_{\rm F}[\omega^2(N^2 - \hat{a}^2)\cos\hat{a}t - \hat{a}^2(N^2 - \omega^2)\cos\omega t] + B_{\rm F}[\omega^2\hat{a}^{-1}(N^2 - \hat{a}^2)\sin\hat{a}t - \hat{a}^2\omega^{-1}(N^2 - \omega^2)\sin\omega t]\}, \quad (3.12)$$

and the postforcing solution (i.e., when $t \ge \sigma$) for $\hat{a} \ne \omega$ is

$$\tilde{u}(t) = \frac{-ilN^2\tilde{F}_\zeta - mlf\tilde{J}}{\mathbf{k}^2\omega^2} - \frac{Dm\hat{a}^2}{k_H^2}\left\{\left(k\omega A_{\rm F} - \frac{lfB_{\rm F}}{\omega}\right)\mathcal{S} - (lfA_{\rm F} + kB_{\rm F})\mathcal{C}\right\}, \quad (3.13)$$

$$\tilde{v}(t) = \frac{ikN^2\tilde{F}_\zeta + mkf\tilde{J}}{\mathbf{k}^2\omega^2} - \frac{Dm\hat{a}^2}{k_H^2}\left\{(kfA_{\rm F} - lB_{\rm F})\mathcal{C} + \left(\frac{kfB_{\rm F}}{\omega} + l\omega A_{\rm F}\right)\mathcal{S}\right\}, \quad (3.14)$$

[4] It can be shown that Eqs. (3.8)–(3.17) are neither singular nor enhanced at $\omega = \hat{a}$.

[5] The special case solutions are given in appendix C.

$$\tilde{w}(t) = \{D\hat{a}^2(A_F\omega\mathcal{S} - B_F\mathcal{C})\}, \quad (3.15)$$

$$\tilde{\Theta}(t) = \frac{mf(iN^2\tilde{F}_\zeta + mf\tilde{J})}{\mathbf{k}^2\omega^2} + DN^2\hat{a}^2\left\{A_F\mathcal{C} + \frac{B_F\mathcal{S}}{\omega}\right\}, \quad (3.16)$$

$$\tilde{P}(t) = \frac{if(iN^2\tilde{F}_\zeta + mf\tilde{J})}{\mathbf{k}^2\omega^2} + \frac{iD\hat{a}^2(N^2 - \omega^2)}{m}\left\{A_F\mathcal{C} + \frac{B_F\mathcal{S}}{\omega}\right\}, \quad (3.17)$$

where $P \equiv p'/\overline{\rho}$, $\Theta \equiv g\theta'/\overline{\theta}$, $\mathcal{S} \equiv \sin\omega t + \sin\omega(\sigma - t)$, and $\mathcal{C} \equiv \cos\omega t - \cos\omega(\sigma - t)$. Equations (3.13)–(3.17) reduce to Eqs. (14a)–(17b) of Luo and Fritts (1993) for an impulsive, hydrostatic, zonal body forcing (i.e., setting $\sigma = 0$, $n = 1$, $\mathbf{k}^2 \simeq m^2$, $\omega^2 \ll N^2$, and $\tilde{F}_y = \tilde{F}_z = \tilde{J} = 0$). The constant amplitude results are obtained by multiplying Eqs. (3.8)–(3.17) by σ.

In general, the body/thermal forcing causes an adjustment process to occur. This process creates a radiated gravity wave field [curly brackets in Eqs. (3.13)–(3.17) with spectral components proportional to the oscillatory terms $\mathcal{S}$ or $\mathcal{C}$] and forces a steady (possibly geostrophic) mean response [all other terms in Eqs. (3.13)–(3.17)]. Here, the ''mean'' response is defined as the postforcing response due to the time-independent spectral components of the solution. Upon taking the inverse Fourier transform, these time-independent spectral components are also time-independent in physical space and make up the steady response after the gravity waves have radiated away apart from the inertial oscillations. This mean response is created entirely by the forcing, since wave–mean flow interactions have been neglected.

In special cases, body forcing results in an insignificant mean response. For example, near the equator and in other circumstances in which f can be neglected, the mean response is small when a zonal body forcing varies negligibly in the meridional direction. If $f = l_c = l = \tilde{F}_y = \tilde{J} = 0$, then there will be no local mean response. However, weak ''waves'' with zero frequency and no horizontal structure (i.e., $k_H^2 = 0$) are created and function as nonlocal mean flows. In this situation, even though there are no Coriolis torques, high-frequency gravity waves are created abundantly from 3D local zonal body forcings (Vadas et al. 2001, unpublished manuscript).

We denote the fast-forcing (or short interval) limit to be $\omega\sigma \ll 1$. In this limit, $\mathcal{S} = \omega\sigma\cos\omega t$ and $\mathcal{C} = -\omega\sigma\sin\omega t$, and the postforcing gravity wave amplitudes are independent of σ and $\hat{a}$. These fast-forcing solutions are equivalent to the impulsive solutions when $\sigma = 0$ and give nearly the same solutions as long as $\omega_c\sigma \ll 1$.

We denote the slow-forcing limit to be $\hat{a} \ll \omega$. In this limit, the postforcing gravity wave amplitudes are greatly reduced because $\hat{a}^2/(\hat{a}^2 - \omega^2)$ is small. This occurs because there is coherent cancellation between gravity waves with frequencies larger than the forcing frequency. For a given source then, we expect very strong damping of gravity wave amplitudes with frequencies larger than the forcing frequency. In addition, $\mathcal{S}$ and $\mathcal{C}$ both equal zero when $\omega = \hat{a}\nu/n$ or $\omega\sigma = 2\pi\nu$, where $\nu = 1, 2, 3, \ldots$ is a positive integer. (Note that this cannot occur in the fast-forcing limit.) Thus, except when $\nu = n$, gravity waves with these particular frequencies will have zero amplitude because of destructive interference from waves created when the forcing turns on and off. These cancellations are averaged out for more realistic temporal distributions built up of many forcings with differing forcing frequencies.

c. Source distributions

Our solutions encompass the response from horizontal and vertical forcings as well as heatings. In general, horizontal and vertical body forces and heatings will accompany mesospheric wave breaking. Meridional forcing can also occur from tidal filtering. The illustrations in this paper, however, are obtained solely from zonal body forcings. We focus on zonal forcings because waves that break in the mesosphere are preferentially filtered zonally in the stratosphere and lower mesosphere, thereby creating primarily zonal momentum flux divergences.

Our choices for the scales and geometries of canonical body forcings in this study are motivated by our knowledge of the characteristic scales of wave–wave and wave–mean flow interactions in the mesosphere (based on current measurements and model studies cited above). The typical vertical scales of such interactions are ~10 km, while horizontal scales are a few tens to hundreds of kilometers. The body forcing accompanying dissipation within a single wave packet would likely have a monopole structure spatially, while gravity wave–tidal interactions imposing variable flux divergence in height would imply a dipole body forcing having the characteristic vertical scale of the tidal modulation (~10 to 15 km between opposing maxima). In a limited way, we also consider the consequences of a dipole distribution of body forcing in latitude, assuming that latitudinal variations in wave sources or filtering conditions may imprint these structures at greater altitudes. Examples of such include gravity wave excitation with opposite directions of propagation northward and southward of a significant tropospheric low pressure system or differential filtering of the gravity wave spectrum by a latitudinally varying tidal or planetary wave velocity field. In these cases, we expect that the scale of the latitudinal dipole would be ~1000 km or more substantially larger than the vertical variations imposed by these same motions. We also consider the dipole-in-longitude distribution for similar reasons.

The spatial distributions of sources representing these choices are

$$F_x(\mathbf{x}) = u_0\left\{\exp\left(-\sum_{i=1}^{i=3}\frac{(x_i - x_{i0})^2}{2\sigma_{x_i}^2}\right)\right\} \times \begin{cases}1, & \text{monopole,}\\ (x_i - x_{i0})/\sigma_{x_i}, & \text{dipole in } x_i,\end{cases} \quad (3.18)$$

where $\mathbf{x} = (x, y, z)$, $\mathbf{x}_0 = (x_0, y_0, z_0)$, and σ_{x_i} is the Gaussian half-width in the x_i direction. (The half-width is defined as the length whereby the function decreases to $e^{-1/2}$ of its maximum value.) The monopole source is either positive or negative, while the dipole sources have equally sized positive and negative regions oriented in x, y, or z. The Fourier transform of $F_x(\mathbf{x})$ is

$$\tilde{F}_x = u_0(2\pi)^{3/2}\sigma_x\sigma_y\sigma_z e^{i\mathbf{k}\cdot\mathbf{x}_0} \times \{\exp(-[k^2\sigma_x^2 + l^2\sigma_y^2 + m^2\sigma_z^2]/2)\} \times \begin{cases}1, & \text{monopole,}\\ ik_i\sigma_{x_i}, & \text{dipole in } x_i.\end{cases} \quad (3.19)$$

These distributions all have ''characteristic'' wavenumbers of

$$k_c \equiv 1/\sigma_x, \qquad l_c \equiv 1/\sigma_y, \qquad m_c \equiv 1/\sigma_z, \quad (3.20)$$

where the subscript ''c'' refers to characteristic. Using Eq. (3.3), we define the characteristic source frequency to be the frequency of a gravity wave associated with these wavenumbers:

$$\omega_c = \left[\frac{(\sigma_x^{-2} + \sigma_y^{-2})N^2 + \sigma_z^{-2}f^2}{\sigma_x^{-2} + \sigma_y^{-2} + \sigma_z^{-2}}\right]^{1/2} = f\left[\frac{1 + (\kappa R)^2}{1 + (\sigma_z\kappa)^2}\right]^{1/2}, \quad (3.21)$$

where $\kappa \equiv k_{HC} = (\sigma_x^{-2} + \sigma_y^{-2})^{1/2}$ is the characteristic horizontal wavenumber and $R \equiv N/m_c f = \sigma_z N/f$ is the Rossby deformation radius. The characteristic source period is defined as

$$\tau_c = 2\pi/\omega_c. \quad (3.22)$$

The shallower (deeper) the source, the lower (higher) the characteristic frequency. We refer to body forces with $\omega_c \gg f$ (or $\kappa R \gg 1$) and $\omega_c \simeq f$ (or $\kappa R \ll 1$) as being ''high'' and ''low'' frequency sources, respectively.

d. Illustrations of radiated gravity waves from body forcings with differing intervals

We illustrate our solutions for a longitudinally symmetric, monopole, zonal body force with a 1-h forcing interval and one cycle.[6] This source is roughly 4.5 km deep and 90 km wide. (However, because the solutions are Boussinesq, spatially scaled results hold for all other monopole zonal forcings with the same aspect ratio, $\sigma_y/\sigma_z = 20$.) Figure 1 shows the solution at various times. The source region exhibits primarily near-inertial and inertial oscillations, and high-frequency gravity waves are observed radiating away in Fig. 1a. This source has the characteristic frequency $\omega_c = 1.0 \times 10^{-3}$ s^{-1} and characteristic source period $\tau_c = 1.7$ h, while the forcing frequency is $\hat{a} = 2\pi/(1\text{ h}) = 1.7 \times 10^{-3}$ s^{-1}. Because the interval is shorter than the characteristic period, the radiation pattern observed is approximately that which would be observed from a purely impulsive forcing. The dash lines show the direction waves with $\omega = \omega_c$ propagate, while the dash-dot-dot-dot lines show the direction waves with $\omega = \hat{a}$ propagate. It is clear that virtually all of the radiated gravity waves have frequencies less than or equal to the characteristic source frequency.

Figure 2 shows the solution for the same source but with a 10-h forcing interval. Because the forcing frequency is much smaller than the characteristic source frequency, this forcing is a slow forcing. As shown in section 2b, the mean response here is identical to the mean response for the body forcing in Fig. 1 (see Fig. 10a for the mean response). However, at $t = 3$ h, gravity waves with $\omega \simeq \omega_c$ (i.e., those following the dash line) are not observed as they were in Fig. 1 at this time. The radiation pattern at $t = 12$ h shows clearly that gravity waves with frequencies greater than the forcing frequency are virtually absent. Thus, nearly all of the radiated gravity waves have frequencies less than or equal to the forcing frequency.

e. Step function in time

If we instead use a step function in the temporal distribution, $\mathcal{F}(t) = 1/\sigma$ for $0 \le t \le \sigma$ and 0 otherwise, then the postforcing vertical velocity is

$$\tilde{w}(t) = \frac{1}{\omega^2\sigma}(A_F\omega\mathcal{S} - B_F\mathcal{C}). \quad (3.23)$$

As noted by Zhu and Holton (1987), because the gravity wave amplitudes are proportional to σ^{-1}, longer forcings excite smaller-amplitude gravity waves. Compare Eq. (3.23) to Eq. (3.15) and note that all of the postforcing solutions are derived from $\tilde{w}(t)$. The amplitudes of the radiated gravity waves for the more realistic temporal forcing represented by Eq. (3.5) is reduced by $\hat{a}^2/(\hat{a}^2 - \omega^2)$ from the amplitudes derived from the step function in time forcing.[7] This factor is approximately equal to 1 for fast forcings but is much less than 1 for slow forcings. The step function in time forcing therefore gives the same solution for fast forcings but overestimates the amplitudes of gravity waves for slow forc-

[6] For all of the illustrations in this paper, N_x, N_y, and N_z are the number of grid points in the x, y, and z directions, respectively, and the gridpoint spacings are $dx = \sigma_x/2$, $dy = \sigma_y/2$, and $dz = \sigma_z/2$. Because a monopole body force is spanned in the x_i direction by $4.5\sigma_{x_i}$, a 2D (3D) monopole source is well-represented here, with 81 (729) grid points within its source area.

[7] For the step function forcing, gravity wave amplitudes are 0 when $\omega\sigma = 2\pi\nu$ for any integer ν.

ings with $\omega_c \gg \hat{a}$ (see Fig. 9). For example, a step function forcing with $\sigma = 5$ h overestimates the amplitudes of gravity waves with periods of 1.7 h by a factor of 8.

For the 3D simulations shown by Zhu and Holton (1987), $\tau_c = 2.5$ h while $\sigma = 1$ h and 3 h—these forcings were not slow. For this reason and because the amplitudes of gravity waves with $\omega \gtrsim \hat{a}$ were overestimated as described above, these authors did not observe the strong gravity wave damping that occurs from more temporally realistic slow body forcings.

f. Postforcing (i.e., $t \geq \sigma$) energetics

Taking the dot product of the momentum equations [Eqs. (2.1)–(2.3)] with $\overline{\rho}\mathbf{v}$, noting that $\mathbf{v} \cdot (\Omega \times \mathbf{v}) = 0$, and using Eqs. (2.4)–(2.5), the energy equation is

$$\frac{\partial}{\partial t}\frac{1}{2}\overline{\rho}\left[\mathbf{v}^2 + \frac{\Theta^2}{N^2}\right] = \overline{\rho}\left[uF_x + vF_y + wF_z + \frac{\Theta}{N^2}J\right]\mathcal{F}(t) - \nabla \cdot (p'\mathbf{v}). \tag{3.24}$$

The quantities in the square brackets on the left-hand side are the kinetic and potential energies per volume, respectively. Using Parseval's theorem, the total energy is

$$E = \frac{1}{2}\overline{\rho}\int\int\int\left[u^2 + v^2 + w^2 + \frac{\Theta^2}{N^2}\right]d\mathbf{x} = \int\int\int \mathcal{E}\, d\mathbf{k}, \tag{3.25}$$

where $\mathcal{E}$ is the spectral energy density and is defined as $\mathcal{E} \equiv \overline{\rho}(|\tilde{u}|^2 + |\tilde{v}|^2 + |\tilde{w}|^2 + |\tilde{\Theta}|^2/N^2)/2$.

We substitute Eqs. (3.13)–(3.16) into Eq. (3.25). The postforcing spectral energy densities due to the mean ($\overline{\mathcal{E}}$) and gravity wave ($\mathcal{E}_{GW}$) responses are

$$\overline{\mathcal{E}} = \frac{\overline{\rho}}{2}\frac{|iN\tilde{F}_\zeta + mfN^{-1}\tilde{J}|^2}{\mathbf{k}^2\omega^2}, \tag{3.26}$$

$$\mathcal{E}_{GW} = \left[\frac{4\hat{a}^4\sin^2(\omega\sigma/2)}{\sigma^2\omega^2(\hat{a}^2-\omega^2)^2}\right]\frac{\overline{\rho}}{2}\frac{\mathbf{k}^2(\omega^2|A_F|^2 + |B_F|^2)}{\omega^2 k_H^2}, \tag{3.27}$$

respectively. In this paper, the overline denotes the value associated with the mean response. The gravity wave spectral energy density decreases rapidly for wave frequencies larger than the forcing frequency, since $\mathcal{E}_{GW}$ is proportional to the temporally dependent factor

$$\left[\frac{4\hat{a}^4\sin^2(\omega\sigma/2)}{\sigma^2\omega^2(\hat{a}^2-\omega^2)^2}\right] \simeq \begin{cases} 1, & \hat{a} \gg \pi n\omega, \\ \dfrac{\sin^2(\omega\sigma/2)}{\pi^2 n^2}\left(\dfrac{\hat{a}}{\omega}\right)^6, & \hat{a} \ll \omega. \end{cases} \tag{3.28}$$

Thus the effect of a finite-interval body forcing is to cut off the generation of gravity waves with frequencies greater than the forcing frequency. Therefore, the total postforcing energy depends on the interval length and forcing frequency for a fixed amount of momentum deposited from a fixed spatial source. As we will show by analogy in the next section, the total system energy varies in this manner because of conservation of momentum.

g. Analogy with a ball-and-block Newtonian system

In this section, we compare our forced atmospheric solutions to the solutions for a forced ball-and-block Newtonian system, since it lends insight to our understanding of the atmospheric solution. Consider a block of mass M and location X resting on a frictionless table. A ball of mass m is attached to the end of a weightless rod of length l, which swings freely from a weightless support rigidly attached vertically to the top of the block. The ball and rod swing as a pendulum with natural frequency ω and make the angle $\xi(t)$ with the vertical. Figure 3 shows the system setup. The block is pushed in the x direction by the force F_{block}. This force has the same temporal evolution as in the atmospheric case [see Eq. (3.5)]. Here, $\hat{a} = 2\pi n/\sigma$, and

$$F_{block}(t) = \frac{(m+M)V_0}{\sigma}\begin{cases}(1-\cos\hat{a}t), & \text{for } 0 \leq t \leq \sigma, \\ 0, & \text{for } t \geq \sigma,\end{cases} \tag{3.29}$$

where V_0 is a constant velocity factor. The solutions to this system are derived in appendix D. The analogy between the atmospheric and ball-and-block solutions is quite good. As with the atmospheric solution, when the total momentum deposited is fixed, the postforcing mean responses do not depend on σ, and the ball-and-block oscillation velocities and the work done by the force (or equivalently, the postforcing total energy of the system) both depend sensitively on σ with the *same* multiplying factors as in the atmospheric case. Thus, as for the atmospheric forcing, if $\omega \ll 2/\sigma$, the energy expended to deposit the momentum can be much greater than that to deposit the same momentum with $\omega \gg \hat{a}$.

The total momentum imparted to the ball and block is $\int_0^\sigma F_{block}(t)\,dt = (m+M)V_0$. If the block is accelerated very slowly (i.e., $\sigma \to \infty$), then the ball and block will accelerate together as $\ddot{X} = F_{block}/(m+M)$, giving the final ball and block velocities of $U = \int_0^\sigma \ddot{X}\,dt = V_0$. (Here, "¨" denotes $\partial^2/\partial^2 t$.) Therefore, only enough work is done by the force to facilitate the mean response: $\overline{E} = (1/2)(m+M)V_0^2$. However, if the forcing is very fast (i.e., $\sigma \to 0$), the ball's velocity is zero just as the forcing finishes. Letting U be the block's velocity and equating the block's momentum to the momentum deposited by the force, $MU = (m+M)V_0$, the block's velocity at $t = \sigma$ is $U = (1 + m/M)V_0$. Thus, U must be larger than V_0 in order that the block initially absorb *all* of the momentum deposited. The total system energy is then $E(t \geq \sigma) = (1/2)MU^2 = (1/2)(m+M)V_0^2[1 +$

m/M], which is an increase of $(1 + m/M)$ over $\overline{E}$. This excess energy provides kinetic and potential oscillatory energy to both the ball and block [see Eq. (D.6)]. Therefore, fast forcing creates an unbalanced system that leads to the creation of compensating oscillatory motions.

A similar argument holds in the atmosphere. We take as an example a longitudinally symmetric zonal body forcing. From Eqs. (3.13)–(3.17), just as the forcing ends (i.e., at $t = \sigma$): i) $\hat{a} \ll \omega$ (slow forcing):

$$\tilde{u} = \overline{\tilde{u}} = \frac{\tilde{F}_x}{\mathbf{k}^2\omega^2}(l^2N^2), \qquad \tilde{v} = \tilde{w} = 0,$$

$$\tilde{\Theta} = \overline{\tilde{\Theta}} = -\frac{\tilde{F}_x}{\mathbf{k}^2\omega^2}(mlfN^2), \tag{3.30}$$

and ii) $\sigma \ll 1/\omega$ (fast forcing):

$$\tilde{u} = \frac{\tilde{F}_x}{\mathbf{k}^2\omega^2}(l^2N^2 + m^2f^2) = \tilde{F}_x > \overline{\tilde{u}},$$

$$\tilde{v} = \tilde{w} = \tilde{\Theta} = 0. \tag{3.31}$$

The total momentum per volume deposited by the body force is $\int \overline{\rho}F_x(\mathbf{x})\mathcal{F}(t)\,dt = \overline{\rho}F_x(\mathbf{x})$. If the forcing is slow, then just enough work is done to accelerate u and θ' to their postforcing mean states. However, if the forcing is very fast, in order to conserve momentum, u must acquire the total momentum of the system [i.e., $u = F_x(\mathbf{x})$] just as the forcing ends. The zonal velocity is therefore larger than the zonal mean wind by $\tilde{F}_x m^2 f^2/(\mathbf{k}^2\omega^2)$, leading to an increase in the system spectral energy density by the amount $\overline{\rho}|\tilde{F}_x|^2 m^2 f^2/(2\mathbf{k}^2\omega^2) = \mathcal{E}_{GW}$ using Eq. (3.27). Thus, a fast forcing creates an unbalanced flow at $t = \sigma$, causing the radiation of gravity waves so as to achieve a balanced mean flow. The fact that it takes more energy to accelerate the atmosphere quickly rather than slowly given a fixed total momentum deposited is therefore due to the requirement of conservation of momentum.

4. Spectral results for radiated gravity waves from 2D zonal body forcings

a. Simple body forcings

The vertical velocity power spectral density (hereafter PSD_{ww^*} or PSD) is defined as

$$\mathrm{PSD}_{ww^*}(k, l, m) = \frac{\displaystyle\int_t^{t+2\pi/\omega} \tilde{w}_{\mathrm{FFT}}\tilde{w}^*_{\mathrm{FFT}}\,dt'}{d\eta N_x N_y N_z \displaystyle\int_t^{t+2\pi/\omega} dt'}, \tag{4.1}$$

for $t \geq \sigma$ (postforcing), where $d\eta$ is the interval length (e.g., dm, dc_x, etc.); N_x, N_y, and N_z are the number of grid points in the x, y, and z directions, respectively; the asterisk denotes taking the complex conjugate; and the fast Fourier transform of the vertical velocity as defined by Eq. (3.1) is $\tilde{w} = dxdydz\tilde{w}_{\mathrm{FFT}}$, where dx_i is the gridpoint spacing in the x_i direction. We temporally average over each gravity wave's period to obtain an average amplitude. All power spectral densities are in units of $(\mathrm{m}^2\ \mathrm{s}^{-2})/d\eta$. The variance content spectra, ωPSD, mPSD, . . . , are in units of meters squared per seconds squared.

Figure 4 shows the radiated gravity wave energy spectrum and variance content spectra as functions of the interval length σ for the same sources as in Figs. 1–2. The solid lines depict the spectra from a nearly impulsive force (since $\sigma \ll 2\pi/\omega_c$), while the dash and dash-dot lines depict the spectra from forces with increasingly longer intervals. The impulsive forcing PSD peaks at the characteristic source period (dotted line in Fig. 4b), while slower forcings peak at successively slower frequencies: $\omega_{\max} \simeq \hat{a}$. As argued in sections 3b and 3f, this is because gravity waves with frequencies greater than the forcing frequency are strongly suppressed. On the other hand, the predominant vertical wavelength of the radiated gravity waves is roughly independent of the interval length and is approximately twice the depth of the body forcing region, $\lambda_z \simeq 9\sigma_z$ (dotted line in Fig. 4d).[8] However, as the interval lengthens, the PSD peak spectral amplitude decreases; its amplitude at $\sigma = 10$ h is decreased by a factor of 50 from its amplitude when the forcing is impulsive. The peak horizontal wavelength is roughly twice the length of the body forcing for the impulsive forcing, $\lambda_y \simeq 9\sigma_y = 180$ km (dotted line in 4c), and is increasingly larger for forcings with increasingly longer durations, peaking at $\lambda_y \simeq 1100$ for $\sigma = 10$ h. This satisfies the dispersion relation for $\omega = \hat{a}$: $\lambda_y \simeq \lambda_z N/\hat{a} \simeq (180\ \mathrm{km})(\sigma/1.7\ \mathrm{h})$. Thus slower forcings create waves with larger horizontal wavelengths. The horizontal phase speed $c_y \equiv \omega/l \simeq N/m$ is approximately independent of the forcing duration because it depends only on the vertical wavelength: $c_y = \lambda_z N/2\pi \simeq 22\ \mathrm{m\ s}^{-1}$. On the other hand, the vertical phase speed $c_z \equiv \omega/m$ decreases as the interval increases beyond the characteristic source period due to the decreasing wave frequencies. The dotted lines in Figs. 4e–f show $c_y = \omega_c 9\sigma_y/2\pi$, and $c_z = \omega_c 9\sigma_z/2\pi$, respectively.

It may be of interest to point out that the gravity waves created from thermal forcings in the troposphere also have vertical wavelengths that are twice the depth of the heating (Salby and Garcia 1987; Alexander et al. 1995). In addition, the gravity waves created from 3D clear-air turbulence (CAT) layers have $|mH| \simeq 1.5$ or $\lambda_z \simeq 6\sigma_z$ for somewhat differing initial conditions (Bühler et al. 1999). Our fast-forcing results agree with those from Bühler et al. (1999) for instantaneously formed CAT layers: $\lambda_x \simeq 9\sigma_x$, using $|kH| \simeq 0.01$ with $H = L/100 = \sqrt{2}\sigma_x/100$.

Figure 5 shows the spectra for fast forcings to be 4.5

[8] Latitudinally symmetric and 3D zonal body forcings also create gravity waves with vertical wavelengths that are approximately twice the vertical extent of the source (Vadas et al. 2001, unpublished manuscript).

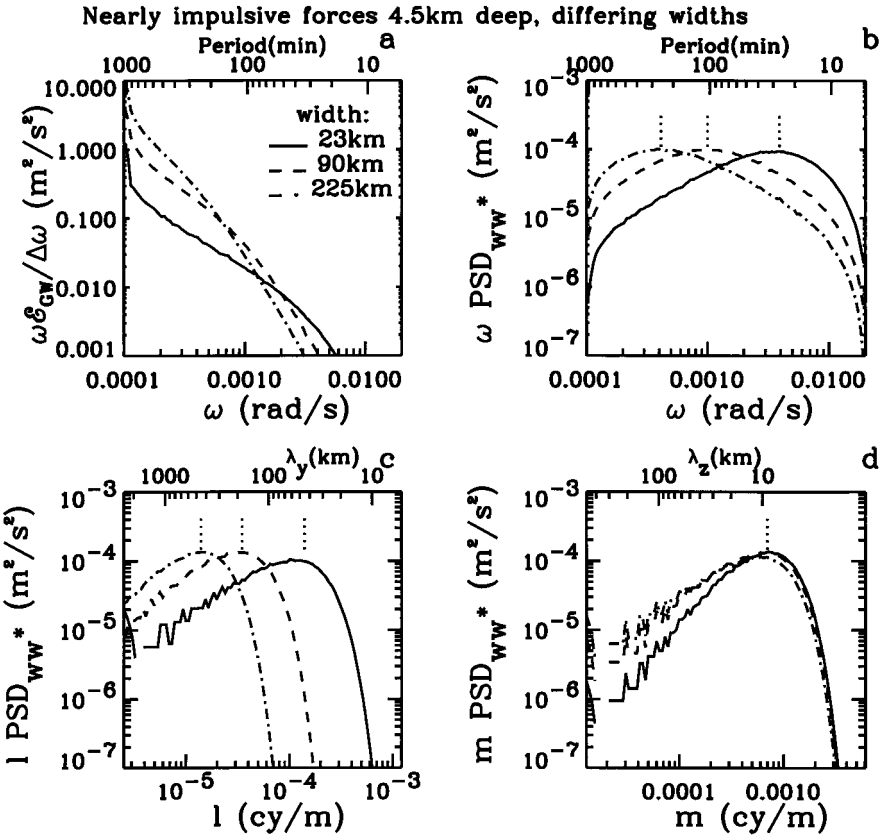

FIG. 5. Spectra in variance content form for longitudinally symmetric monopole zonal body forcings. The spectra of the sources with $\sigma_y = 5$ km, $\sigma_y = 20$ km, and $\sigma_y = 50$ km are shown with solid, dash, and dash-dot lines, respectively. The dotted lines are located at (b) $\omega = \omega_c$, (c) $\lambda_y = 9\sigma_y$, (d) and $\lambda_z = 9\sigma_z$. For these sources, $u_0 = 1$ m s^{-1}, $\sigma_z = 1$ km, $n = 1$, $\sigma = 0.1$ h, $t = \sigma$, and $N_y = N_z = 1024$. All forcings are essentially impulsive.

km deep and with varying horizontal extents. Because these forcings are nearly impulsive, the spectral variations are due entirely to the changing aspect ratios. As shown by the dotted lines, the PSD spectra peak at the characteristic source period, vertical wavelengths that are twice the depth of the body forcing, and horizontal wavelengths that are twice the horizontal extent of the body forcing.

To test these conclusions, we show the peak spectral values in Fig. 6 for a wide variety of body forcings with differing aspect ratios and forcing frequencies. The dotted lines indicate where the peak frequency equals ω_c in Figs. 6a–b and where the peak horizontal and vertical wavelengths equal twice the width and depth of the forcing in Figs. 6c–d, respectively. From Fig. 6a, the peak frequency equals the forcing frequency for slow forcings. For fast forcings, however, the peak frequency equals the characteristic source frequency. In Fig. 6b, we determine where this transition occurs. For a forcing frequency greater than $\simeq 5\omega_c$, the peak frequency equals ω_c. As the forcing frequency decreases from this value, the peak frequency decreases slowly. When $\hat{a} \simeq \omega_c$, the spectra peaks at $\omega_c/2$. But as the forcing frequency decreases further, the peak frequency rapidly approaches the forcing frequency—it equals the forcing frequency when $\hat{a} \lesssim \omega_c/10$ (as long as $\hat{a} \geq f$). When $\hat{a} < f$ [as happens for the three slowest forcings for $\sigma_y = 50$ km (asterisks)], the gravity wave frequencies are $\omega \simeq f$. Figure 6c–d show that for fast forcings, the peak horizontal and vertical wavelengths are about twice the width and depth of the forcing, respectively. However, for slow forcings, the peak vertical wavelength decreases somewhat, whereas the peak horizontal wavelength increases dramatically.

Therefore for fast forcings, the peak frequency is the characteristic source frequency, and the peak horizontal and vertical wavelengths are twice the width and depth of the source, respectively. For slow forcings, the peak frequency is the forcing frequency, the peak vertical wavelength is slightly smaller than twice the depth of the source, and the peak horizontal wavelength is much larger than twice the width of the source. The increase in horizontal wavelength is needed in order for these lower-frequency waves to satisfy the dispersion relation with roughly the same vertical wavelength.

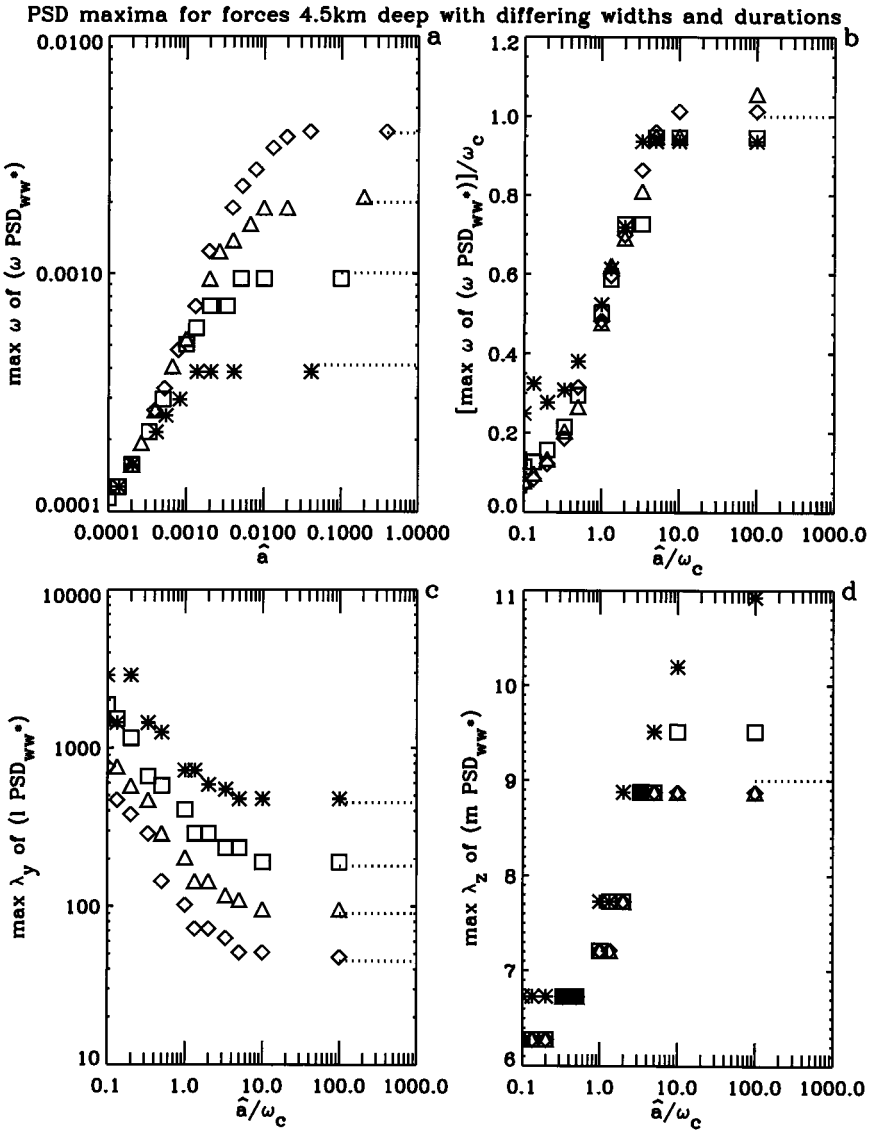

FIG. 6. (a) Maximum ω of ωPSD_{ww*}, (b) maximum ω of ωPSD_{ww*} divided by ω_c, (c) maximum λ_y of $l\text{PSD}_{ww*}$, and (d) maximum λ_z of $m\text{PSD}_{ww*}$. The longitudinally symmetric monopole zonal body forcings all have $\sigma_z = 1$ km and $n = 1$. The diamonds, triangles, squares, and asterisks show the results for $\sigma_y = 5$, 10, 20, and 50 km, respectively. The dotted lines are located at (a), (b) $\omega = \omega_c$, (c) $\lambda_y = 9\sigma_y$, and (d) $\lambda_z = 9\sigma_z$, respectively. For this illustration, $N_y = N_z = 2048$, and the evaluation times are $t = 2\sigma$ for $\sigma/\tau_c < 1$ and $t = \sigma$ otherwise. This figure does not depend on the forcing amplitude u_0.

b. Body forcings with more realistic temporal distributions

Up until now, our illustrations involved single cycle, $n = 1$ forcings. But wave dissipation processes are likely much more temporally variable than a single $\sin^2(\ldots t)$ forcing. We superpose 10 forcings with differing values of σ, n, u_0, and t_0 (i.e., the starting time) in order to simulate a more realistic temporal distribution with added variability on 1–3-h timescales. We regard this as conservative given that variability can also occur at higher frequencies (e.g., Holton and Alexander 1999). In Fig. 7, we compare the spectra of radiated gravity waves from two spatially identical monopole, zonal sources with $2\pi/\omega_c = 1.7$ h $= 105$ min but with differing temporal variability. The total zonal momentum deposited in each case is the same. The body force parameters used to generate the solid lines in this figure are given in Table 2. The forcing periods range from $\sigma/n = 0.5$ h through 10 h, although the largest amplitudes occur for periods of $\sigma/n \simeq 1$ h through 5 h. This combination of forcing functions was chosen as an example of how temporal variability can alter the solution. The dotted

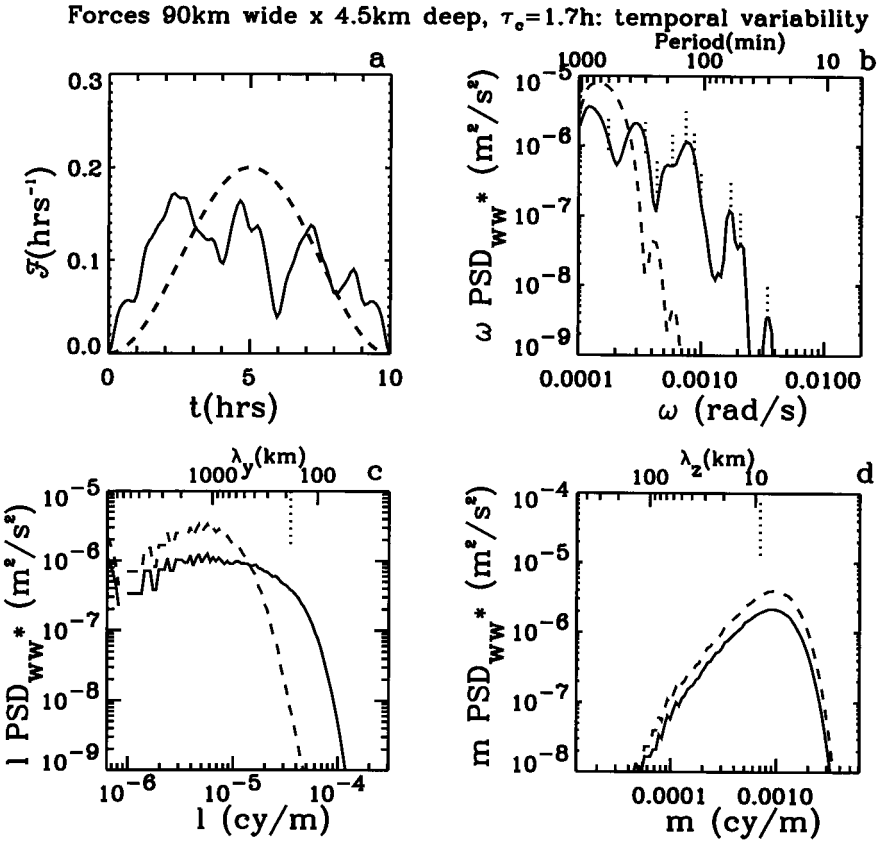

FIG. 7. Dependence of spectra on differing temporal evolutions when forcing envelope is ''slow.'' (a) Temporal distribution, $\mathcal{F}(t)$, for a single $n = 1$, $\sigma = 10$ h forcing (dash line), and temporal distribution for a more complicated evolution that composed of 10 forcings with an overall envelope of 10 h (solid line). The parameters used to generate the complicated temporal evolution are displayed in Table 2. (b), (c), (d) Postforcing spectra in variance content form for longitudinally symmetric monopole zonal body forcings with $\sigma_y = 20$ km, $\sigma_z = 1$ km, $n = 1$, and $u_0 = 1$ m s^{-1}. The spectral results are shown as dash (solid) lines for the corresponding dash (solid) line displaying $\mathcal{F}(t)$ in (a). The dotted lines show the location of the forcing frequencies for the complicated temporal evolution in (b). The dotted lines in (c) and (d) are located at $\lambda_y = 9\sigma_y$ and $\lambda_z = 9\sigma_z$, respectively. For this illustration, $t = 10$ h and $N_y = N_z = 1024$.

lines in Fig. 7b show the forcing frequencies. There are ''spikes'' in the PSD at the highest forcing frequencies (i.e., at 30, 50, and 60 min). The extra high-frequency temporal variability results in significantly higher amplitudes for radiated gravity waves with periods smaller than 6 h (or $\omega > 3 \times 10^{-4}$ s^{-1}). For example, at wave periods of 1–2 h, spectral amplitudes are increased by approximately 100 in this example. These high-frequency waves are expected to propagate more easily to greater altitudes. It is important to note, however, that temporal variability is only expected to significantly enhance the amplitudes of higher-frequency gravity waves when the period of the envelope (in this case, 10 h) is of order or larger than the characteristic source period. If the period of the envelope is much smaller than the characteristic source period, then any added high-frequency temporal variability will do little to alter the gravity wave amplitudes. In Fig. 7c, the PSD is broadly distributed in horizontal wavelength, with a low wavelength cutoff at twice the horizontal extent of the source. The vertical wavelengths, however, do not depend on the temporal variability. Thus, the radiated gravity waves have vertical wavelengths that are twice the depth of the source and a range of horizontal wavelengths that are of order or larger than twice the horizontal extent of the source.

c. Body forcings with spatial variability

Because wave field dissipation (especially wave breaking) may be intermittent and patchy, the body forcing distributions will likewise be patchy rather than smoothly distributed (Andreassen et al. 1998; LeLong and Dunkerton 1998; Holton and Alexander 1999; Franke and Robinson 1999). For example, Fig. 8 of Holton and Alexander (1999) suggests that there may be many spatially localized regions of wave breaking within the overall wave field. Thus, source regions will not, in

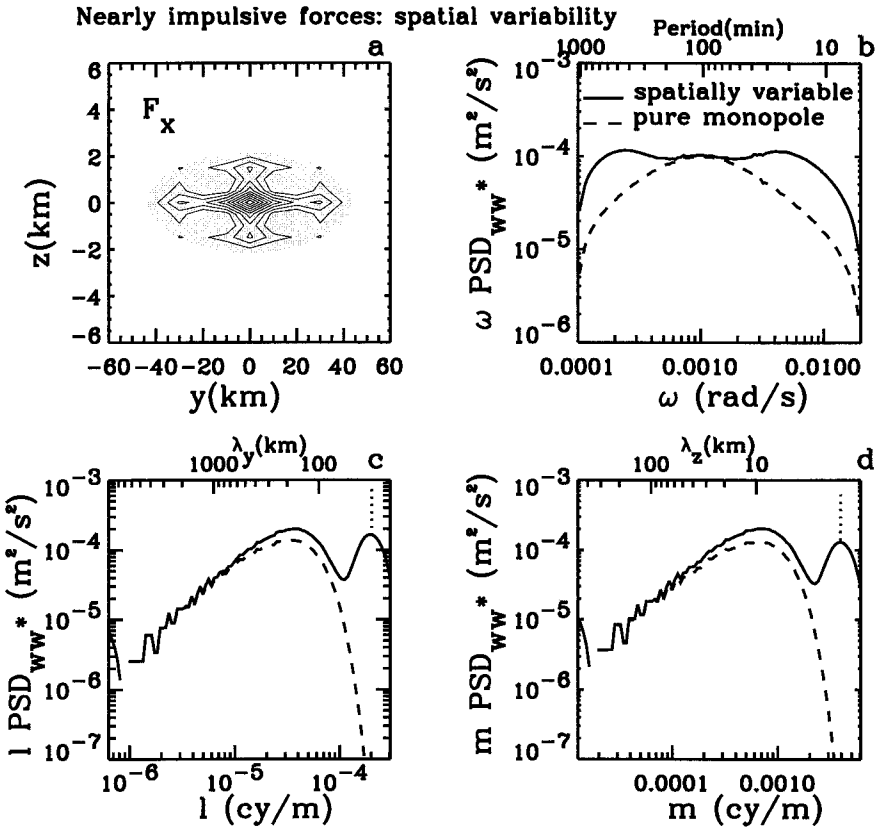

FIG. 8. Effect of spatial variability on a monopole longitudinally symmetric zonal body forcing. (a) Outline of the pure monopole forcing at 10% of its maximum (shaded). Solid contour lines show the outline of the spatially variable source [Eq. (4.2)] at 10% increments of its maximum. This source is a monopole source with added horizontal and vertical variability at $\pi\sigma_y/2$ and $\pi\sigma_z/2$, respectively. (b), (c), (d) PSD_{ww*} for the spatially variable source [i.e., Eq. (4.2)] with solid lines and for the pure monopole source with dash lines. Here, $\sigma_y = 20$ km, $\sigma_z = 1$ km, $\sigma = 3$ min, $n = 1$, $u_0 = 1$ m s^{-1}, $t = 2\sigma$, and $N_y = N_z = 1024$. The dotted lines show the location of the added variability at $\lambda_y = \pi\sigma_y/2 = 31$ km in (c) and at $\lambda_z = \pi\sigma_z/2 = 1.6$ km in (d). Both forcings are essentially impulsive.

general, resemble the idealized monopole sources we have considered above. In order to investigate the effect of spatial variability of a localized body forcing region on the spectra of radiated waves, we consider the zonal forcing with added horizontal and vertical wavelength variabilities at $\pi\sigma_y/2$ and $\pi\sigma_z/2$, respectively:

$$F_x(\mathbf{x}) = \left\{1 + \cos\left(\frac{4[y - y_0]}{\sigma_y}\right) + \cos\left(\frac{4[z - z_0]}{\sigma_z}\right)\right\} u_0 \times \exp\left(-\frac{(y - y_0)^2}{2\sigma_y^2} - \frac{(z - z_0)^2}{2\sigma_z^2}\right). \quad (4.2)$$

In Fig. 8a, we show the monopole forcing (shading) as well as the spatially variable source with added variability at $\lambda_y = 31$ km and $\lambda_z = 1.6$ km using Eq. (4.2) (contour lines). In each case, the total momentum deposited is the same. The spectra are shown in Figs. 8b–d as solid lines for the spatially variable source and dash lines for the pure monopole source. The spectra are not sensitive to the temporal portion of the body forces because they are essentially impulsive. Thus, the difference between the solid and dash lines is due entirely to the source's added spatial variability. These spatial variabilities add very substantial components to the spectrum at $\lambda_y = 31$ km and $\lambda_z = 1.6$ km (dotted lines in Figs. 8c–d, respectively, and the spectrum is broadened considerably in frequency from 20 min to 8.3 h, consistent with the added spatial variability. The meridional variability creates deeper forcings and thus the added higher-frequency components, while the vertical variability creates shallower forcings and thus the added lower-frequency components. Finally, the energy is substantially higher for the spatially variable forcing. In this example, the total kinetic plus potential energy in radiated gravity waves is increased by 3.7 for the spatially variable forcing (not shown). Thus, spatial variability can substantially enhance the radiated gravity wave amplitudes at frequencies higher and lower than the characteristic frequency of the overall source.

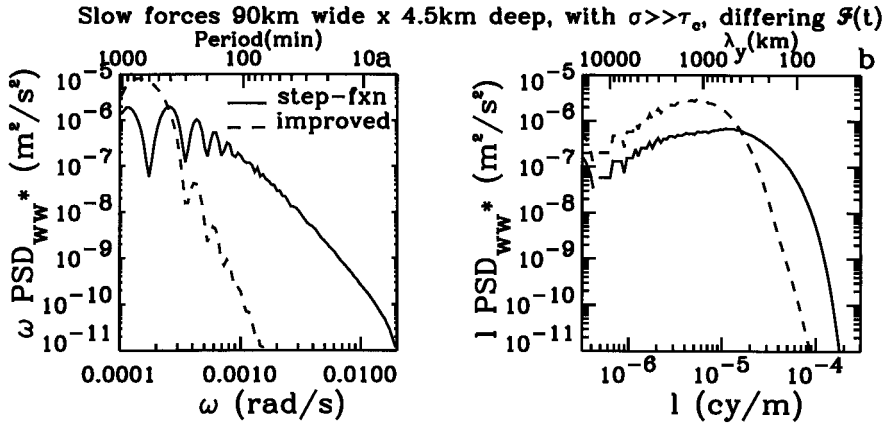

FIG. 9. Spectra in variance content form for slow monopole longitudinally symmetric zonal body forcings with the same spatial distributions but with differing temporal evolutions, $\mathcal{F}(t)$. The spectra for the step function temporal distribution is shown as solid lines, while the spectra for the improved temporal distribution [see Eq. (3.5)] is shown as dash lines. For this illustration, $\sigma_y = 20$ km, $\sigma_z = 1$ km, $n = 1$, $u_0 = 1$ m s^{-1}, $t = \sigma = 10$ h, and $N_y = N_z = 2048$.

d. Body forcings from step function in time temporal variability

In section 3e, we found that the step function in time solutions are essentially identical to the ''improved'' postforcing solutions [i.e., Eqs. (3.13)–(3.17)] when the forcings are fast. This is because gravity waves will only respond to temporal fluctuations a few times larger or smaller than the characteristic source period. However, we found that for slower forcings, the step function in time forcing overestimates the amplitudes of gravity waves with frequencies larger than the forcing frequency. This is because higher-frequency components are needed to turn on and off the step function instantaneously, regardless of the forcing duration. This slow-forcing effect is illustrated in Fig. 9. There, we show the PSD for the step function forcing (solid lines) and improved forcing (dash lines). The characteristic period and forcing periods are $\tau_c = 1.7$ h and $\sigma = 10$ h, respectively. The most striking difference between the spectra is that the average amplitude of the step function spectra does not drop off until $\omega \geq 2\pi/100$ min $\simeq \omega_c$, whereas the improved temporal forcing drops off quickly for $\omega \gtrsim \hat{a} = 2\pi/600$ min.[9] The peak vertical wavelengths of either forcing is about twice the depth of the forcing (not shown). The horizontal wavelengths of the step function waves are correspondingly smaller.

5. Postforcing mean responses

a. Illustrations from 2D zonally symmetric zonal forcings

In Fig. 10, we illustrate the mean responses for zonally symmetric monopole zonal forces: Fig. 10a, high-frequency source with horizontal width of 90 km; Fig. 10b, low-frequency source with horizontal width of 4500 km. Both sources are 4.5 km deep and are outlined by the lightly filled contours at the $\geq$10% level. The mean response in Fig. 10a is the same as the mean response in Figs. 1 and 2.

The zonal mean wind, $\overline{u}$, for the high-frequency monopole source is virtually the same as that of the source $F_x(\mathbf{x})$. Dual, vertically stacked residual circulation cells are created during the forcing, with southward motion throughout the source region (see Figs. 1a–b and 2a–b). Because a fluid parcel's potential temperature relative to the surrounding fluid is lower (higher) when it moves up (down) adiabatically in an isothermal atmosphere, regions of upwelling (downwelling) have lower (higher) potential temperatures. Of particular interest is that the potential temperature response is ''broadened'' in latitude with half-width, denoted Δ_y, of $\Delta_y \simeq 100$ km, even though the latitudinal half-width of the source is only $\sigma_y = 20$ km. By ''broadening,'' we mean that a spatial dimension of the mean response is larger than that of the source. However, neither mean response is broadened vertically. In addition to the broadened latitudinal half-width, the mean potential temperature decreases much more slowly than the source in latitude: $\overline{\theta'} \sim \exp(-|y - y_0|/\Delta_y)$.

For the low-frequency monopole source, there are several important differences. First, the main eastward zonal jet is weakened considerably (by a factor of 5) and is broadened considerably vertically. In addition, there are ''countersigned'' westward jets with amplitudes that are 20% of the amplitude of the main eastward jet for $|y - y_0| \gtrsim 1.5\sigma_y$. By counter-signed, we mean that the resulting mean winds are in the *opposite* direction than the forcing is applied. The potential temperature is also broadened vertically, and no mean response is broadened latitudinally. These effects are due to the

[9] The other difference is the zero in the step function spectrum at $\omega = \hat{a}$, which is absent in the improved spectrum. However, this and the other zeros would not be present from more realistic temporal forcings because of averaging.

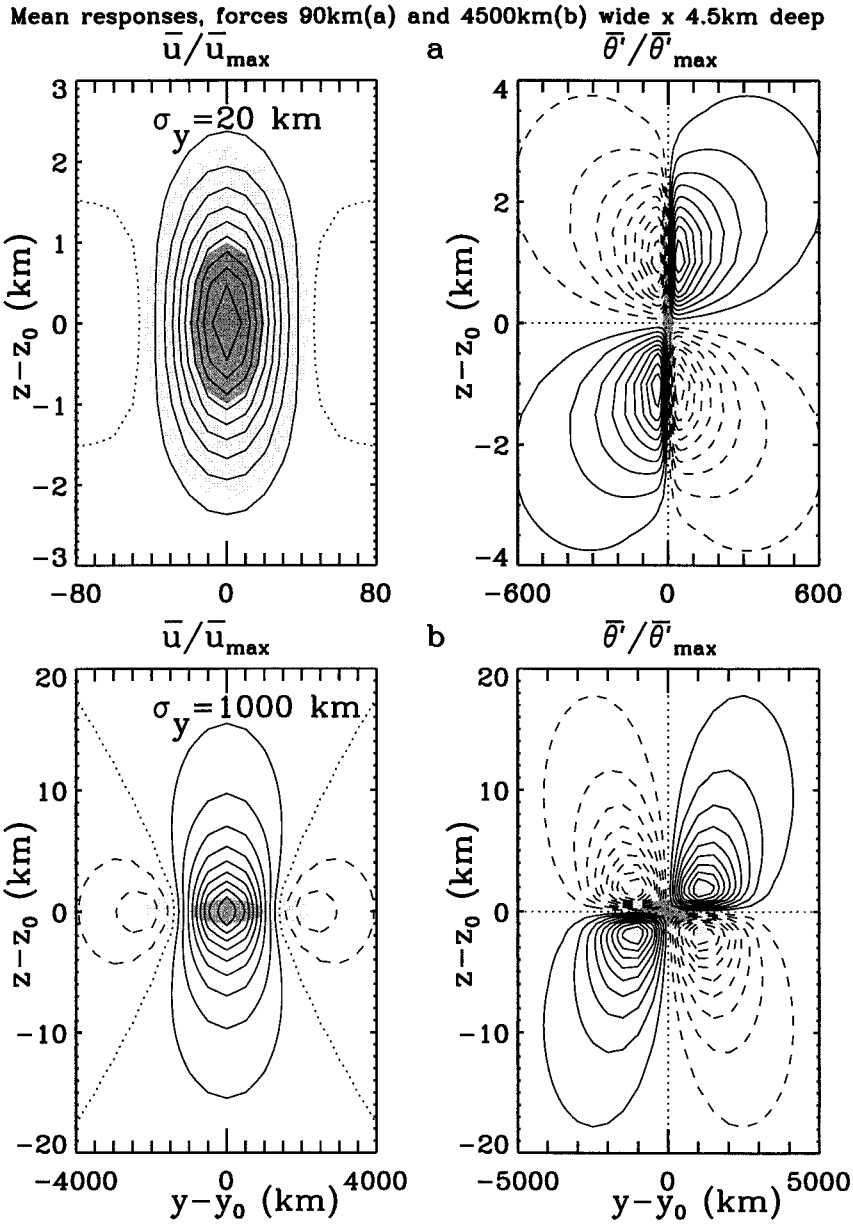

FIG. 10. Postforcing, mean responses for monopole longitudinally symmetric zonal forcings with $\sigma_z = 1$ km and $u_0 = 1$ m s^{-1}. (a) High-frequency source with $\sigma_y = 20$ km. (b) Low-frequency source with $\sigma_y = 1000$ km. The plots on the left show the zonal mean wind, $\overline{u}$, scaled by their maximum values, $\overline{u}_{\max}$, while the plots on the right show the mean, potential temperature, $\overline{\theta'}$, scaled by their maximum values, $\overline{\theta'}_{\max}$. The values of $\overline{u}_{\max}$ and $\overline{\theta'}_{\max}$ for (a) are 0.91 m s^{-1} and 1.2 K, respectively, while the values of $\overline{u}_{\max}$ and $\overline{\theta'}_{\max}$ for (b) are 0.17 m s^{-1} and 1.9 K respectively. The solid lines indicate values from 0.1 to 1.0 with 0.1 increments, the dash lines indicate the values from -0.1 to -1.0 with -0.1 increments, and the dotted lines indicate the values 0. The lightly shaded region indicates where the source is $\geq$10% of its maximum value, while the darkly shaded region indicates where the source is greater than $\exp(-0.5) = 0.61$ of its maximum value. For this illustration, $t = \sigma = 10$ h, $n = 1$, and $N_y = N_z = 512$. Note that this figure is identical (but with proportionately differing values of $\overline{u}_{\max} \propto u_0$ and $\overline{\theta'} \propto u_0$) for any forcing amplitude.

zonal Coriolis torque, which decelerates the forming zonal wind during the forcing. This zonal Coriolis torque is created from the meridional residual circulation, which is formed during the forcing as a result of the meridional Coriolis torque.[10] Thus, the countersigned zonal wind regions are formed from the meridional residual circulation ''back-reacting'' onto the zonal wind. From Eq. (2.1), northward flows move eastward while southward flows move westward in the Northern Hemisphere. Thus, as the main meridional southward jet accelerates westward, the strength of the main eastward zonal jet is reduced in the immediate forcing region, and weak westward-moving jets are created in the northern and southern wings where the eastward body forcing is small. In addition, the meridional northward jets above and below the forcing region expand the zonal jet vertically to the extent that the residual circulation broadens vertically (not shown). Likewise, the potential temperature response broadens in the vertical because the areas of vertical motion are spread vertically. For both the zonal mean wind and mean potential temperature responses, the vertical half-widths, denoted Δ_z, are about $\Delta_z = 2.5$ km, an increase of 2.5 over the vertical half-width of the source.

To determine which physical effects balance the zonal body forcing, we do a term-by-term analysis of the zonal momentum equation when $\sigma \to \infty$ and $\hat{a} \to 0$ so that only mean responses are created. Substituting Eqs. (3.8)–(3.12) into the Fourier transform in space of Eq. (2.1), the integrated zonal momentum terms [which sum to $\tilde{F}_x$ using $\mathbf{k}^2\omega^2 = (k^2 + l^2)N^2 + m^2f^2$] are

$$\int_0^\sigma \frac{\partial \tilde{u}}{\partial t}\, dt = \overline{\tilde{u}} = \frac{l^2N^2}{\mathbf{k}^2\omega^2}\tilde{F}_x,$$

$$\int_0^\sigma (-ik\tilde{P})\, dt = \frac{k^2N^2 - klfN^2\sigma/2}{\mathbf{k}^2\omega^2}\tilde{F}_x,$$

$$\int_0^\sigma (-f\tilde{v})\, dt = \frac{m^2f^2 + klfN^2\sigma/2}{\mathbf{k}^2\omega^2}\tilde{F}_x. \qquad (5.1)$$

The zonal acceleration only balances the body forcing exclusively when the source is high frequency and $l_c \gg k_c$: $\partial u/\partial t \simeq F_x(\mathbf{x})\mathcal{F}(t)$, giving a zonal mean flow that equals the source $\overline{u} \simeq F_x$. But if the source is high frequency and $k_c \gg l_c$ or if the source is low frequency, then the pressure gradient and/or the zonal Coriolis torque instead supply the zonal momentum balance: $(\partial p'/\partial x)/\overline{\rho} - fv \simeq F_x(\mathbf{x})\mathcal{F}(t)$. In particular, 1) the zonal Coriolis torque balances a zonally symmetric, low-frequency body force, $\int_0^\sigma v\, dt \simeq -F_x(\mathbf{x})/f$, and drives the meridional wind of the residual circulation; and 2) the zonal pressure gradient balances a body force when rotation can be neglected and $k_c \gg l_c$: $\int_0^\sigma (\partial p'/\partial x)\, dt \simeq \overline{\rho}F_x(\mathbf{x})$.

[10] The Coriolis torque is $fv\mathbf{i} - fu\mathbf{j}$ from Eqs. (2.1)–(2.2), so the zonal and meridional Coriolis torques are fv and $-fu$, respectively.

b. *Theoretical analysis of mean forcing solution characteristics*

Here, we derive general features of the mean responses by examining the spectral solutions. We show that mean wind responses in the opposite direction to the forcing are common for many types of body forces. We also show that mean responses are typically significantly broadened spatially (over the spatial extent of the source) in one direction only; the mean responses from low-frequency sources are only broadened vertically, while the mean responses from high-frequency sources are only broadened horizontally (they are broadened zonally if $\sigma_x \ll \sigma_y$ and are broadened meridionally if $\sigma_y \ll \sigma_x$). In addition, we derive a formula [Eq. (5.3)] that estimates the broadened half-width of a mean response from a given source. We show that the extent of the broadening is determined by the spatial dimensions of the source but not on the extent of the source in the direction that broadens. These results explain the mean response features highlighted in Fig. 10. Essentially, we find that the mean responses often do not resemble the sources spatially because of mass conservation. This includes the action of Coriolis torques when rotation is important.

The spectral solution for the mean response generated from a given source consists of the Fourier transform of the source times wavenumber factors in the numerator (e.g., l^2, kl) divided by the following wavenumber factors in the denominator: $(k^2 + l^2)N^2 + m^2f^2$. Wavenumber factors in the numerator represent derivatives of the source in physical space and determine spatial solution symmetries for simple sources. For example, the meridional mean wind exhibits dipole behavior in both x and y for a 3D monopole zonal forcing because $\overline{\tilde{v}} \propto kl\tilde{F}_x$ (see also Fritts and Luo 1992; Luo and Fritts 1993). In addition, the zonal mean winds from zonal monopole sources can be countersigned when $|y - y_0| \gtrsim \sigma_y$. This follows because $\overline{\tilde{u}} \propto l^2\tilde{F}_x/\mathbf{k}^2\omega^2$, so that when $\mathbf{k}^2\omega^2 \neq l^2N^2$, the zonal mean wind is proportional to

$$-\frac{d^2}{dy^2}\exp[-(y - y_0)^2/2\sigma_y^2]$$

$$= \frac{1}{\sigma_y^2}\left[1 - \frac{(y - y_0)^2}{\sigma_y^2}\right]\exp[-(y - y_0)^2/2\sigma_y^2]. \qquad (5.2)$$

This quantity is positive in the source region and negative outside of the source region. For example, if a zonally symmetric, low-frequency zonal force is eastward, then although the zonal mean wind will be eastward in the source region, the zonal mean wind will be westward outside of the source region where $|y - y_0| \gtrsim \sigma_y$ (e.g., Fig. 11[11]). Due to cancellation of l^2 factors in the numerator and denominator, however, zonal forces with $\sigma_y \lesssim R$ and $\sigma_y \lesssim \sigma_x$ will not have significant

[11] The neglected factor of l^2 in the solution denominator changes the exact location somewhat.

countersigned regions. A similar conclusion, that is, that the meridional mean winds created from meridional monopole sources are countersigned for $|x - x_0| \gtrsim \sigma_x$ when $\mathbf{k}^2\omega^2 \neq k^2N^2$, follows because $\tilde{v} \propto k^2\tilde{F}_y/\mathbf{k}^2\omega^2$. And analogously, meridional forces with $\sigma_x \lesssim R$ and $\sigma_x \lesssim \sigma_y$ will not have significant countersigned regions.

On the other hand, uncancelled wavenumber factors in the denominator, $\mathbf{k}^2\omega^2 = k^2N^2 + l^2N^2 + m^2f^2$, represent spatial ''broadening'' of the mean response. By broadening we mean that the spatial extent of the mean response in one direction is larger (potentially much larger) than the spatial extent of the source in that same direction. Consider a high-frequency source with a meridional extent that is much smaller than the zonal extent, that is, $\sigma_y \ll \sigma_x$. In this case, the denominator of the mean spectral solutions can be approximated as $\mathbf{k}^2\omega^2 \simeq N^2(l^2 + a^2)$, where $a \simeq (k_c^2 + R^{-2})^{1/2}$ is constant. Upon taking the inverse spatial transform of the mean spectral solutions, when $|l| < a$, the contributions to the integral are multiplied by the constant factor $1/N^2a^2$. But when $|l| \gg a$, the contributions to the integral are very small. Thus, meridional wavenumbers larger than a will not influence the broadened mean solutions significantly. The ''characteristic wavenumber'' of the mean response then is a and is *smaller* than the characteristic wavenumber of the source l_c. We therefore estimate that the mean response from this source is *broadened* meridionally with the resulting half-width of $\simeq 1/a$. The extent of the broadening is determined by whichever is smaller, σ_x or R, and does not depend upon the value of σ_y. If $\sigma_x \ll R$, then the mean response will have approximately equal horizontal extents, unlike the source. But if $\sigma_y = \sigma_x$ or $\sigma_y = R$, then only very small or negligible meridional broadening occurs. Analogous conclusions are made for high-frequency sources with $\sigma_x \ll \sigma_y$ and for low-frequency sources.

Therefore, the mean response created from 1) a high-frequency source with $\sigma_x \ll \sigma_y$ can only be broadened in x, 2) a high-frequency source with $\sigma_y \ll \sigma_x$ can only be broadened in y, and 3) a low-frequency source can only be broadened in z. The spatially broadened half-widths for these three distinct classes of sources are approximately[12]

$$\Delta_x \simeq \frac{1}{2(\sigma_y^{-2} + R^{-2})^{1/2}} \quad \text{for sources with } \omega_c \gg f \quad \text{and} \quad \sigma_x \ll \sigma_y,$$

$$\Delta_y \simeq \frac{1}{2(\sigma_x^{-2} + R^{-2})^{1/2}} \quad \text{for sources with } \omega_c \gg f \quad \text{and} \quad \sigma_y \ll \sigma_x,$$

$$\Delta_z \simeq \frac{f}{2N\kappa} \quad \text{for sources with } \omega_c \simeq f. \tag{5.3}$$

[12] The factor of 1/2 gives the actual half-widths for sources with $\Delta_y/\sigma_y \gtrsim 5$. It gradually increases to 1.0 below this value as the broadening effect becomes decreasingly important (not shown).

Plugging in the source half-widths, we see that the latitudinally and vertically broadened mean responses depicted in Fig. 10 are in agreement with Eq. (5.3).

All spatial broadening occurs because of mass conservation [i.e., Eq. (2.5)]. Setting $\hat{a} = 0$ to obtain only the mean flow effects, this integrated continuity equation in spectral space becomes

$$\int_0^\sigma dt[(k\tilde{u}) + \lfloor l\tilde{v} \rfloor + \{m\tilde{w}\}] = \frac{\tilde{F}_x}{\mathbf{k}^2\omega^2}[(kl^2N^2\sigma/2) + \lfloor -lm^2f - kl^2N^2\sigma/2 \rfloor + \{m^2lf\}]. \tag{5.4}$$

Inside the square brackets, the terms within the inner ( ), $\lfloor\ \rfloor$, and { } are due to the zonal, meridional, and vertical velocity gradient contributions to mass conservation, respectively. For zonally symmetric forces, Coriolis torques work to ensure mass continuity between the meridional and vertical winds during the forcing, which may result in vertical or meridional broadening of the mean responses. But when rotation is unimportant, there is instead a balance between the zonal and meridional winds, which may result in horizontal broadening of the mean responses.

For special sources (e.g., monopole and dipole sources), certain mean wind/potential temperature fields may be broadened while others may not be due to the coincidental cancellation of wavenumber factors in the numerator and denominator. Using Eqs. (3.19) and (3.13)–(3.17), we summarize the mean postforcing responses that are broadened for monopole and dipole zonal forces in Table 3. A check denotes that the mean solution is broadened in the x, y, or z direction relative to the source, and a dash denotes that the response is not broadened. Most of the mean responses broaden. Table 3 agrees with Figs. 10–12.

From Eqs. (3.13), (3.14), and (3.16), the zonal mean wind only equals a zonal force (i.e., $\overline{\tilde{u}} \simeq \tilde{F}_x$) if the source is high frequency and $l_c \gtrsim k_c$. In this situation, the zonal mean wind will not be broadened and will not have significant countersigned regions. (However, an additional heating and meridional force with $l_c \gtrsim k_c$ results in meridionally broadened zonal mean wind contributions.) Likewise, the meridional mean wind only equals a meridional force (i.e., $\overline{\tilde{v}} \simeq \tilde{F}_y$) if the source is high frequency and $k_c \gtrsim l_c$. And the mean potential temperature only equals a thermal forcing (i.e., $\overline{\tilde{\Theta}} \simeq \tilde{J}$) if the source is low frequency. Thus, a zonal, meridional, and thermal forcing with similar spatial scales will never result in zonal mean winds, meridional mean winds, and mean potential temperature responses that are all simultaneously identical to each of their respective forcings unless $\sigma_x \simeq \sigma_y \simeq R$.

As an example of our findings, Zhu and Holton (1987) found in their studies that the induced mean fields are

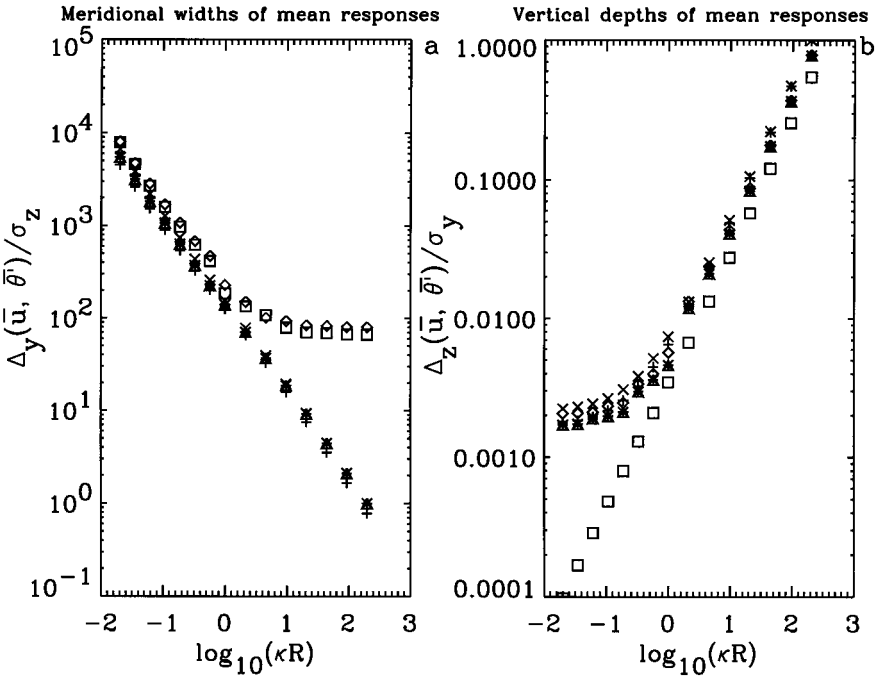

FIG. 11. Meridional and vertical half-widths of the mean responses from longitudinally symmetric zonal forcings. The half-widths of the zonal mean winds for the monopole, dipole-in-*y*, and dipole-in-*z* sources are represented by the symbols ×, +, and *, respectively. The half-widths of the mean potential temperatures for the monopole, dipole-in-*y* and dipole-in-*z* sources are represented by diamonds, triangles, and squares, respectively. In all cases, $\sigma_z = 1$ km, $t = \sigma = 10$ h, and $n = 1$. For $\sigma_y \leq 200$ km, $N_y = 4096$ and $N_z = 128$, and for $\sigma_y \geq 200$ km, $N_y = 128$ and $N_z = 4096$. This figure does not depend on the forcing amplitude.

confined to the 3D forcing region. However, they chose characteristic scales for which no broadening occurs: $\sigma_x = \sigma_y = 200$ km and $R = 1000$ km (see their p. 625). Because this is a high-frequency source and $\sigma_x = \sigma_y$, the mean response does not broaden. Fritts and Luo (1992) noticed only a very small amount of vertical broadening in their 2D mean responses. Significant vertical broadening did not occur because they chose $\sigma_y = R = 100$ km (see their p. 683). Luo and Fritts (1993) chose a 3D source with $\sigma_x = 1000$ km, $\sigma_y = R = 100$ km, for which there is negligible broadening because the smallest and second smallest of σ_x, σ_y, or R are the same (see their p. 105). Thus, the mean responses were not broadened and did not have significant countersigned regions in these papers due to the coincidental choices of the characteristic source scales. Indeed, these comparisons highlight the insights obtained with an analytic formulation of the body forcing problem.

c. *Spatially broadened half-widths from 2D zonally symmetric zonal forces*

Figure 11 shows the calculated meridional and vertical half-widths for the main features of the zonal mean wind and potential temperature responses for longitudinally symmetric zonal forces. Meridional broadening only occurs for high-frequency deep sources (i.e., $\sigma_y \ll R$), while vertical broadening only occurs for low-frequency shallow sources (i.e., $R \ll \sigma_y$). The only mean responses that broaden meridionally are the potential temperature responses for the monopole and dipole-in-*z* sources, while all of the mean responses broaden vertically except for the potential temperature response for the dipole-in-*z* source. These results agree with Table 3. In agreement with Eq. (5.3), the meridionally broadened mean responses satisfy $\Delta_y/\sigma_z \simeq 80$–100 regardless of the horizontal extent of the sources, and the vertically broadened mean responses satisfy $\Delta_z/\sigma_y \simeq 0.002$–0.0025 regardless of the vertical extent of the sources.

d. *Illustrations from 3D zonal forces*

Figure 12 shows the zonal mean winds from 3D zonal forces. Lightly shaded contours show where sources are ≥ 10% of their maximum values. In Fig. 12a, the source is high frequency with $\sigma_y \ll \sigma_x$ and results in a zonal mean wind, which closely resembles the source, and a meridional mean wind and mean potential temperature that broaden meridionally (not shown). The zonal mean wind that results from a high-frequency source with σ_x

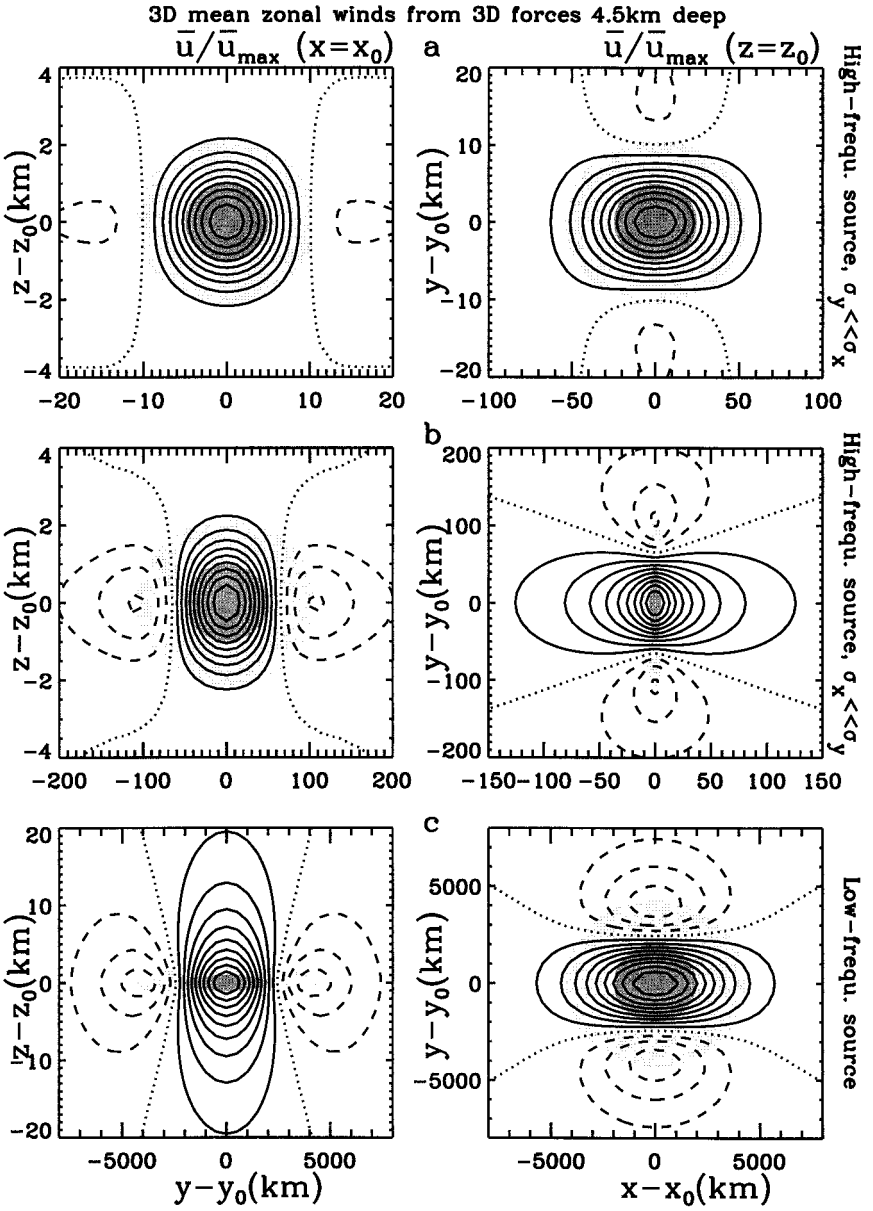

FIG. 12. Slices of the zonal mean winds three different 3D, monopole, zonal forcings with $u_0 = 1$ m s^{-1}. (a) The response for a high-frequency monopole with $\sigma_x = 25$ km, $\sigma_y = 5$ km, and $\sigma_z = 1$ km ($N_x = N_z = 64$ and $N_y = 512$). (b) The response for a high-frequency monopole with $\sigma_x = 5$ km, $\sigma_y = 50$ km, and $\sigma_z = 1$ km ($N_x = 512$ and $N_y = N_z = 64$). (c) The response for a low-frequency monopole with $\sigma_x = \sigma_y = 2000$ km and $\sigma_z = 1$ km ($N_x = N_y = 64$ and $N_z = 512$). The left-hand (right-hand) column shows the zonal mean winds on the slice $x = x_0$ ($z = z_0$). Each contour plot is scaled by its maximum zonal mean wind, which is 0.83 m s^{-1}, 0.086 m s^{-1}, and 0.069 m s^{-1} for (a), (b), and (c), respectively. The contour line and shading intervals are as in Fig. 10. For all illustrations, $t = \sigma = 10$ h and $n = 1$. Note that this figure is identical (but with proportionately differing values of $\bar{u}_{max}$) for any forcing amplitude.

$\ll \sigma_y$ is shown in Fig. 12b. Two countersigned zonal jets are aligned meridionally about the source center for $|y - y_0| \gtrsim 1.5\sigma_y$ [see Eq. (5.2)], and the zonal mean wind is broadened zonally with half-width $\Delta_x \simeq 25$ km, consistent with Eq. (5.3) using $\sigma_x = 5$ km. Thus, within a factor of 2, broadening results in approximately equal horizontal half-widths, and the zonal mean wind decays more slowly in $|x - x_0|$ than the source, a consequence of the source being Gaussian. The zonal mean wind that results from a low-frequency source is shown in Fig. 12c. As in Fig. 12b, countersigned jets for $|y - y_0| \simeq 1.1\sigma_y$ are present and are aligned meridionally. In addition, vertical broadening occurs with half-width $\Delta_z \simeq 5$ km, consistent with Eq. (5.3) using $\sigma_z = 1$ km.

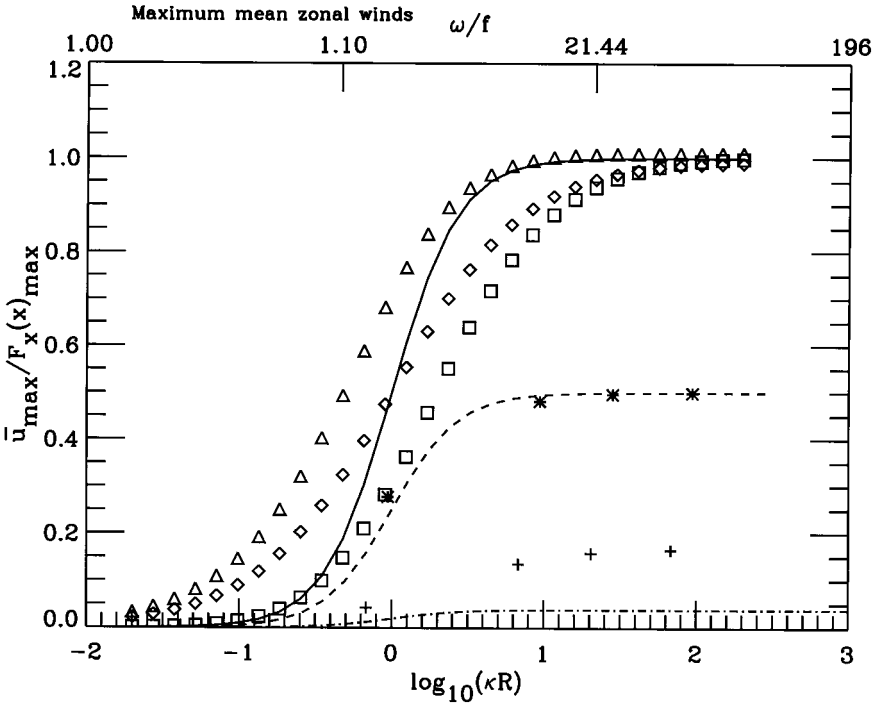

FIG. 13. The maximum zonal mean wind divided by the maximum amplitude of the source created from zonal body forces with $t = \sigma = 0.1$ h and $n = 1$. The diamonds, triangles, and squares indicate the results for 2D longitudinally symmetric monopole, dipole-in-y, and dipole-in-z sources, respectively. The asterisks and plus symbols indicate the results for 3D monopole sources with $\sigma_x = \sigma_y$ and $\sigma_x = \sigma_y/5$, respectively. The solid, dash, and dash-dot lines indicate the estimated fraction using Eq. (5.5) for $k_c/l_c = 0$, 1, and 5, respectively. The top horizontal axis displays several values of 2D characteristic source frequencies. For all of the 2D forces, $N_y = N_z = 512$. For the 3D forces, $N_x = N_y = 256$ and $N_z = 64$ for the sources with $\sigma_x = \sigma_y$, and $N_x = 512$ and $N_y = N_z = 64$ for the sources with $\sigma_x = \sigma_y/5$. This figure does not depend on the forcing amplitude.

e. *Illustrations of zonal force estimates using characteristic scales*

By simply calculating the spectral amplitudes at the characteristic source scales, it turns out that we can estimate reasonably well the fraction of energy in gravity waves, the zonal and meridional mean wind amplitudes, and the mean potential temperature. This is useful when a source is dominated by single horizontal and vertical scales. For purposes of estimating general features of the solution then, we assume that the characteristic source wavenumbers and frequency are the dominant peaks in the source spectrum with negligible spread. Evaluating the postforcing mean spectral components of Eqs. (3.13), (3.14), and (3.16) at the characteristic wavenumbers for a zonal force, the maximum 3D mean zonal and meridional winds and potential temperature are estimated to be

$$\overline{u}_{\max} \simeq F_x(\mathbf{x})_{\max} \frac{(R/\sigma_y)^2}{1 + (\kappa R)^2}, \tag{5.5}$$

$$\overline{v}_{\max} \simeq -F_x(\mathbf{x})_{\max} \frac{R^2/\sigma_x\sigma_y}{1 + (\kappa R)^2}, \tag{5.6}$$

$$\overline{\theta'}_{\max} \simeq -\frac{f\overline{\theta}F_x(\mathbf{x})_{\max}}{g} \frac{R^2/\sigma_y\sigma_z}{1 + (\kappa R)^2}, \tag{5.7}$$

respectively, where the maximum amplitude of the zonal source is denoted $F_x(\mathbf{x})_{\max}$. In Fig. 13, we show the actual and estimated maximum zonal mean winds for many different source shapes and sizes. The longitudinally symmetric forcings are represented by triangles, diamonds, and squares, while the 3D forcings are represented by asterisks and pluses. The estimated maximum mean winds reflect the actual maximum mean winds reasonably well because the main feature is the transition that occurs at $\kappa \simeq R^{-1}$ between very small wind speeds for shallow forcings to very large wind speeds for deep forcings. The actual transition is more broadly distributed in frequency because the estimate does not account for the true spectral contents of the sources.

Figure 14 shows the maximum mean potential temperatures. The maximum of this function occurs at the Rossby deformation radius and is 30°–70°C for monopole and dipole forcings with $F_x(\mathbf{x})_{\max} \simeq 10$ m s^{-1}. The broadening of the mean potential tempera-

ture response in frequency leads to a reduction in the amplitude at $\kappa \simeq R^{-1}$ by approximately a factor of 2.

During the adjustment that accompanies zonal forcing, energy is partitioned between mean and gravity wave responses. Evaluating Eqs. (3.26)–(3.27) at the characteristic source scales, the estimated fraction of energy in radiated gravity waves is

$$\frac{E_{\rm GW}}{\overline{E} + E_{\rm GW}} \simeq \frac{m_c^2[\mathbf{k}_c^2 f^2 + k_c^2(N^2 - f^2)]}{m_c^2[\mathbf{k}_c^2 f^2 + k_c^2(N^2 - f^2)] + l_c^2 N^2 \mathbf{k}_c^2\{\sigma\omega_c(1 - \omega_c^2/\hat{a}^2)/[2\sin(\omega_c\sigma/2)]\}^2}, \tag{5.8}$$

where $E_{\rm GW}$ and $\overline{E}$ are the energies due to the oscillatory and mean responses, respectively. For fast forcings (i.e., $\sigma \ll 2/\omega_c$), the estimated fraction of energy is

$$\frac{E_{\rm GW}}{\overline{E} + E_{\rm GW}} \simeq \left[1 + \frac{l_c^2 \mathbf{k}_c^2 N^2}{m_c^2[\mathbf{k}_c^2 f^2 + k_c^2(N^2 - f^2)]}\right]^{-1} \tag{5.9}$$

$$\simeq \left[1 + \frac{l_c^2 N^2}{m_c^2 f^2 + k_c^2 N^2}\right]^{-1} = \frac{1 + (R/\sigma_x)^2}{1 + (\kappa R)^2}$$

$$\text{if } \mathbf{k}_c^2 \simeq m_c^2, \tag{5.10}$$

where the second line holds when $\omega_c \ll N$ from Eq. (3.21).

Figure 15 displays the $\log_{10}$ of the estimated fraction of energy in gravity waves using Eq. (5.8) for longitudinally symmetric zonal forcings (Fig. 15a), 3D zonal forcings with $\sigma_x = \sigma_y$ (Fig. 15b), and $\sigma_x = \sigma_y/10$ (Fig. 15c). The dash line shows $\omega_c = \hat{a}$ using [Eq. (3.21)]

$$\kappa R = (N/f)[(\omega_c^2 - f^2)/(N^2 - \omega_c^2)]^{1/2}. \tag{5.11}$$

Forcings well above (below) this line are fast (slow). For forcings that are fast, the production of gravity waves is highly favored by 1) low-frequency sources and 2) high-frequency sources with $\sigma_x \lesssim \sigma_y$. On the other hand, high-frequency longitudinally symmetric sources highly favor the production of mean responses, with the transition occurring at the Rossby deformation radius. This result, as applied to longitudinally symmetric sources, is consistent with the results of previous work (Walterscheid and Boucher 1984; Zhu and Holton 1987; Fritts and Luo 1992); as σ_y decreases relative to σ_z, the source becomes deeper, and pressure forces increasingly oppose the Coriolis force during the forcing so that the zonal flow becomes increasingly balanced by the forcing. From Eq. (2.8), the postforcing potential vorticity induced from the zonal body forcing (hereafter PV) is $\zeta_\theta(t \geq \sigma) - \zeta_\theta(t = 0) = -\partial F_x/\partial y \propto u_0/\sigma_y$. Therefore, for increasing values of $\log_{10}(\kappa R)$ in Fig. 15, the PV increases (since σ_x and σ_y decrease while u_0 and σ_z remain constant) and $E_{\rm GW}/(\overline{E} + E_{\rm GW})$ decreases. This agrees with the results of Bühler et al. (1999) in the impulsive limit. Figures 15b–c show that fast high-frequency 3D zonal forcings produce gravity waves very efficiently, greatly enhancing the production of radiated gravity waves over ''equivalent'' (i.e., same l_c and R but with $k_c = 0$) zonally symmetric zonal forces.

We also observe destructive interference patterns. These are smeared out if more realistic temporal variability is taken into account or if the estimate could account for the finite spectral width of the source. Additionally, the fraction of energy in gravity waves drops off very sharply at and beyond the second zero, that is, when $\sigma \geq 4\pi/\omega_c$. For all slow forcings well below the dash line, there is virtually no estimated gravity wave response.

Figure 16a (Fig. 16b) shows the $\log_{10}$ of the fraction of energy in radiated gravity waves with frequencies $\omega > \omega_c/3$ for 2D (3D) monopole zonal forcings. We also show the $\log_{10}$ of the fraction of energy for all gravity waves (including inertial oscillations) generated from 3D sources with $\sigma_x = \sigma_y$ in Fig. 16c. As above, the dash lines indicate where $\omega_c = 2\pi/\sigma$. The difference between Figs. 16b and 16c is that for high-frequency sources, Fig. 16b shows the fraction of the energy in high frequency waves, while Fig. 16c shows the total fraction of energy in waves. Because high-frequency zonally symmetric monopole sources radiate a substantial amount of energy as inertial oscillations and near-inertial gravity waves, the fraction of the total energy in radiated gravity waves does not decrease very quickly for $\sigma > 2\pi/\omega_c$ (Fig. 16c). The agreement between the integrated fraction of energy in Figs. 16a,b with the estimated fraction shown in Figs. 15a,b is fairly good. Therefore, the estimated fraction of energy in gravity waves given by Eq. (5.8) is a fairly accurate, simple, first-order approximation as to how the energy is partioned in a wave dissipation event. This type of formula may be useful as a correction to general circulation model (GCM) parameterization of gravity wave effects on the mean flow.

6. Summary and discussion

In this paper, we derived the 3D Boussinesq, *f*-plane solutions to horizontal and vertical body forces and heatings applied over the temporal interval length σ in a nonsheared, constant buoyancy frequency background. The interval length ranges from zero to infinity. This generalizes past solutions in that 1) the solutions cover impulsive forcings through infinitesimally slowly vary-

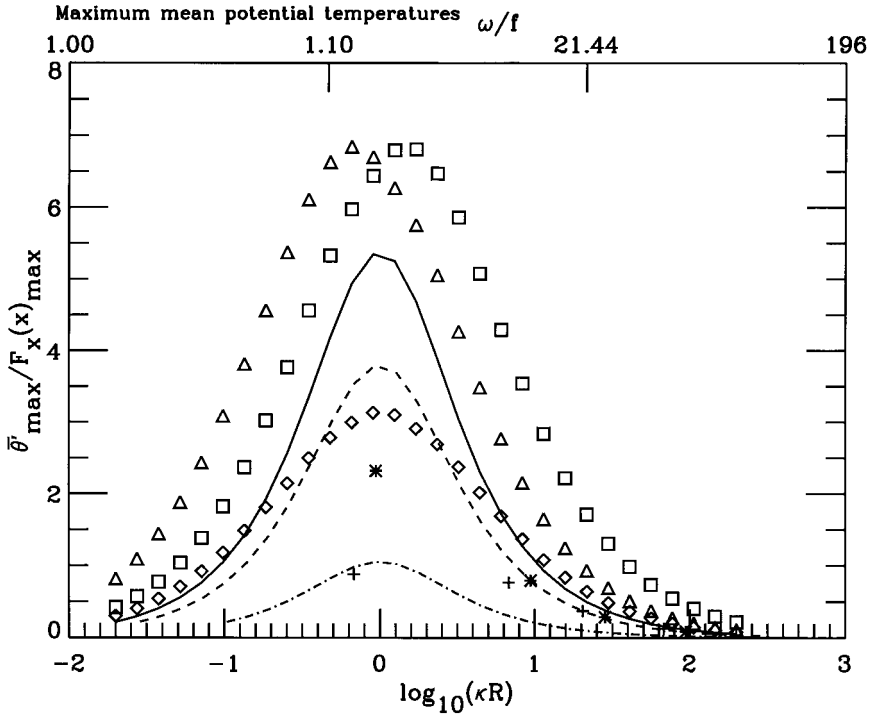

FIG. 14. Same as in Fig. 13 but displaying instead the maximal mean potential temperatures. The estimated quantities here are obtained from Eq. (5.7) and are multiplied by 1/2. This figure does not depend on the forcing amplitude u_0.

ing forcings (depending on the forcing frequency and interval lengths chosen) and 2) the forces are applied in a continuous (but not necessarily slow) manner, that is, as $\sin^2(\hat{a}t/2)$, where $\hat{a}$ is the forcing frequency. This characterizes the high-frequency waves created from nonimpulsive forces better than a step function in time forcing. This model determines properties associated with the creation (not propagation) of gravity waves from body forces and heatings in an idealized unsheared background. Indeed, strong shears and vertical changes in N will likely alter this generated spectrum in ways not currently understood. The primary focus of this paper is the exploration of the mean and gravity wave responses that arise from differing 2D and 3D zonal body forces (scales, frequencies, amplitudes, etc.). These results are summarized in the following paragraphs, and implications pertaining to these results follow.

Suppose a given source region has half-widths σ_x, σ_y, and σ_z in the x, y, and z directions, respectively. This source has characteristic frequency $\omega_c = ([\kappa^2 N^2 + f^2/\sigma_z^2]/[\sigma_z^{-2} + \kappa^2])^{1/2}$, where $\kappa = (\sigma_x^{-2} + \sigma_y^{-2})^{1/2}$ is the characteristic horizontal wavenumber. The deeper the source, the larger the characteristic source frequency. The spectrum of radiated gravity waves that results from a forcing depends on the spatial character of the source and forcing frequency content factors. The maximum amplitudes of radiated gravity waves for a given source results from impulsive forcings. The temporal character of the forcing modifies the impulsive spectrum by greatly reducing the amplitudes of gravity waves with frequencies greater than the forcing frequency. This is due to the coherent cancellation of gravity waves with frequencies larger than the forcing frequency. For impulsive forcings, the PSD (vertical velocity power spectral density) peaks at the characteristic frequency, whereas if the forcing frequency is smaller than the characteristic frequency ($f \leq \hat{a} \ll \omega_c$), then the PSD peaks at the forcing frequency.

Virtually independent of the forcing frequency (and therefore regardless of the dominant frequency of the created waves), the vertical wavelength of waves generated from a given zonal body force is approximately twice the depth of the source. And if the forcing interval is smaller than the source's characteristic period, the horizontal wavelength is twice the horizontal extent of the source. On the other hand, if the forcing frequency is much smaller than the source's characteristic frequency, then the PSD peak amplitudes decrease dramatically, and the dominant horizontal wavelength is lengthened to be twice the horizontal extent of the source times $\omega_c/\hat{a}$. For example, for scales representative of expected forcing by convectively or orographically generated gravity waves (vertical and horizontal extents $\sim$10 km and $\sim$ a few tens or hundreds of kilometers, respectively), the horizontal wavelengths of radiated gravity waves will be tens to hundreds of kilometers if the forcing duration is less than 2 h and will be greater

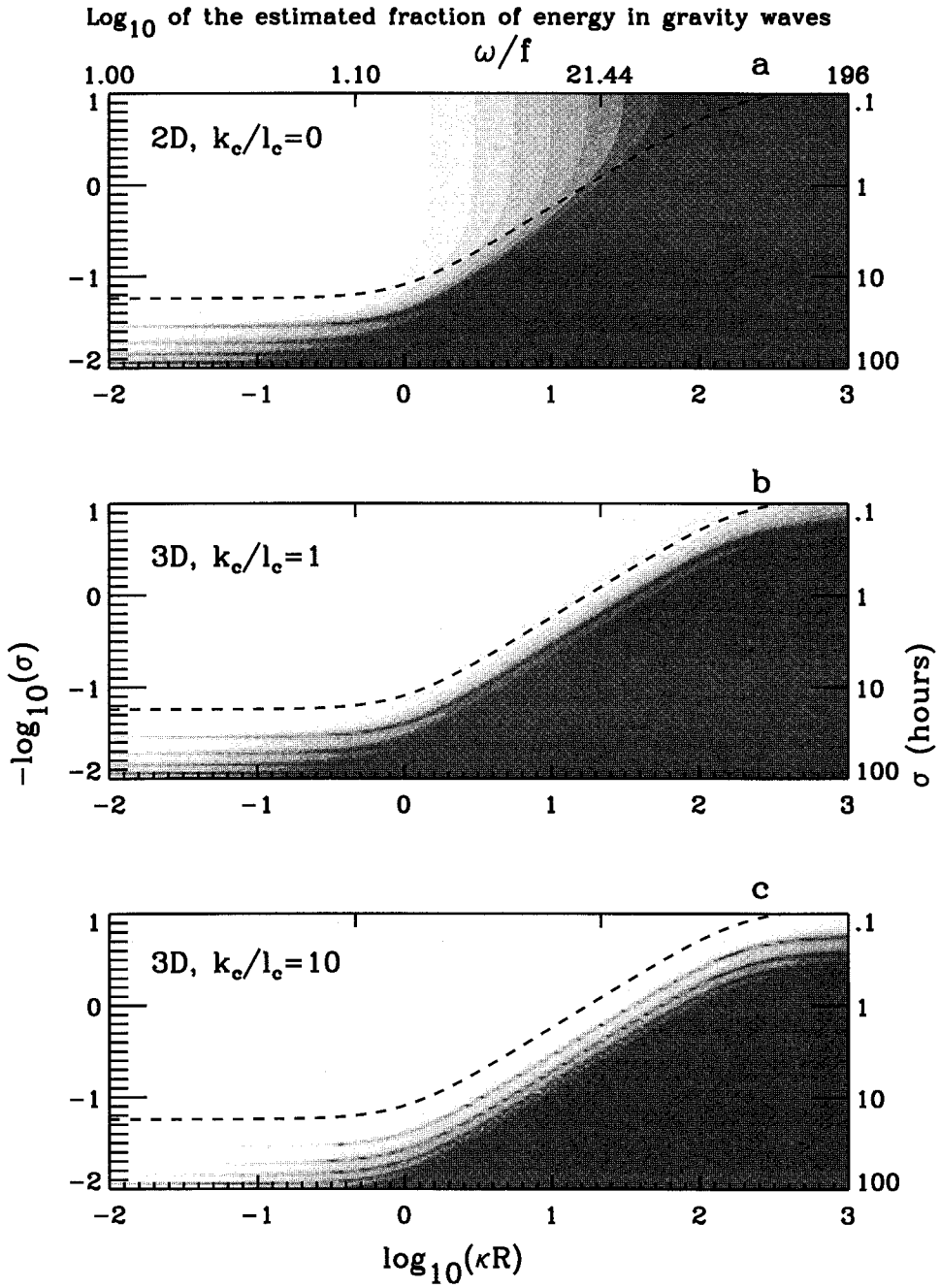

FIG. 15. The $\log_{10}$ of the estimated fraction of the energy in radiated gravity waves from zonal forces in increments of -0.5 using Eq. (5.8) for one forcing cycle (i.e., $n = 1$). The lightest regions are when this estimated fraction is ≥ 0.316 and the darkest regions are when this fraction is $\leq 1\times 10^{-4}$. We show these results for $k_c/l_c = 0$, 1, and 10 from top to bottom, respectively. The dash lines indicate where $\omega_c = 2\pi/\sigma$. The labels for ω/f at the top of (a) shows the the corresponding 2D characteristic source frequencies. This figure does not depend on the forcing amplitude.

than this amount by $\simeq(\tau_{\hat{a}}/2$ h) if the forcing period, $\tau_{\hat{a}} \equiv 2\pi/\hat{a}$, is greater than 2 h. In both cases, the vertical wavelengths of the radiated gravity waves is about 20 km.

Temporal and spatial variability broaden the spectrum of radiated waves. Spatial variability broadens and enhances both the frequency and wavenumber PSD spectra. Temporal variability can lead to greatly enhanced gravity wave amplitudes at higher frequencies, perhaps as much as 10 or 100 times as much as the temporally smoothed force for a nonimpulsive force with long temporal envelopes. Therefore, pa-

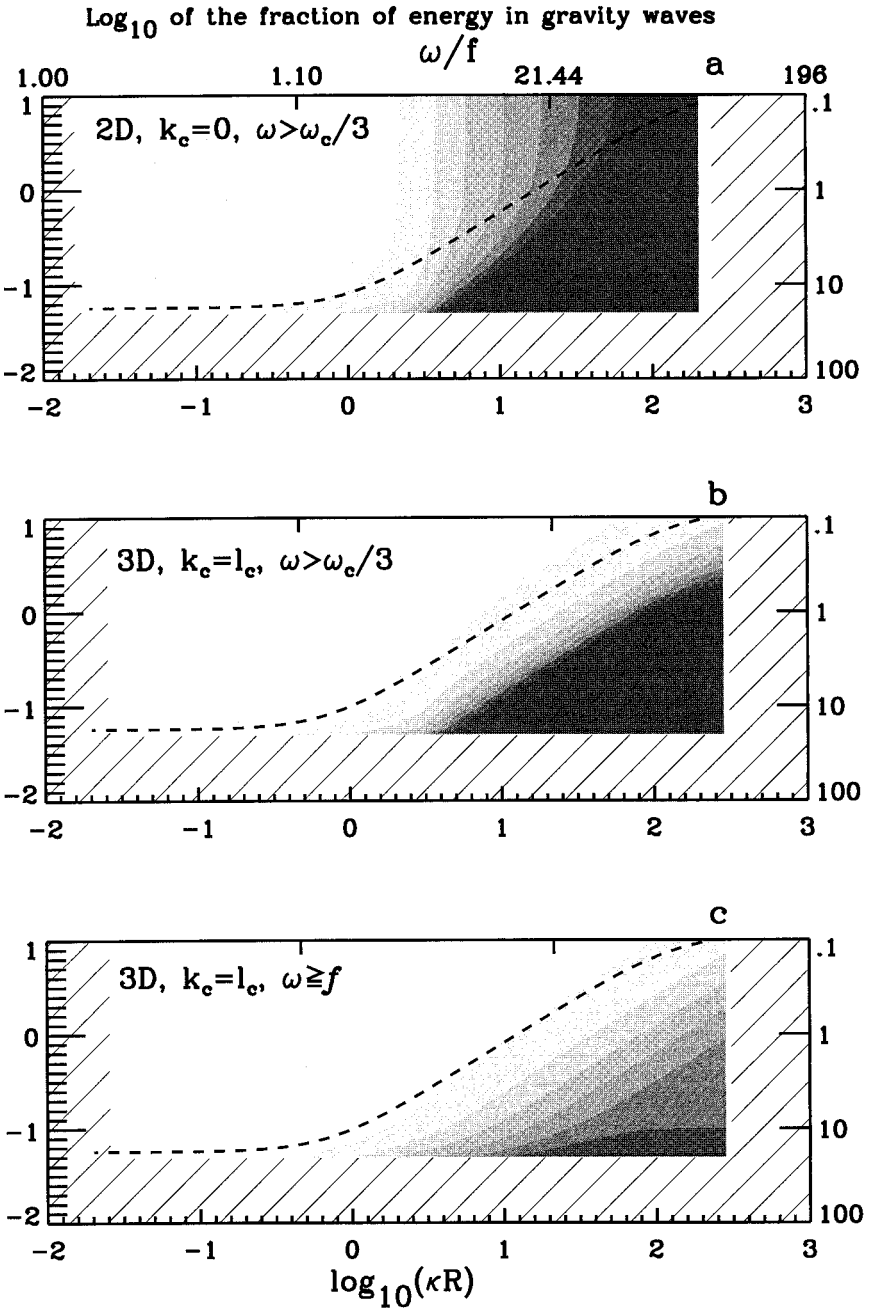

FIG. 16. The $\log_{10}$ of the fraction of the energy in radiated gravity waves from zonal forces in increments of -0.5 for longitudinally symmetric and 3D monopole sources. (a) Results from 2D longitudinally symmetric forces. Here, we only display the fraction of energy in gravity waves that satisfy $\omega > \omega_c/3$. (b) Results from 3D forces with $\sigma_x = \sigma_y$. Here, we only display the fraction of energy in gravity waves that satisfy $\omega > \omega_c/3$. (c) Results from 3D forces with $\sigma_x = \sigma_y$. Here, we display the total fraction of energy in gravity waves (i.e., $\omega \geq f$). Here, $\sigma_z = 1$ km, $n = 1$, σ_y ranges from 1 to 10 000 km, and the quantities were calculated at $t = \sigma$. The forcing intervals range from 0.1 to 20 h. The lightest regions are when this fraction is ≥ 0.316 and the darkest regions are when this fraction is $\leq 1 \times 10^{-4}$. The dash lines indicate where $\omega_c = 2\pi/\sigma$. Simulations for parameters in the hatched regions were not performed. For all 2D sources, $N_y = N_z = 512$. For the 3D sources, $N_x = N_y = 64$ and $N_z = 512$ for the sources with $\sigma_x/\sigma_z \leq 200$, and $N_x = N_y = 256$ and $N_z = 64$ for the sources with $\sigma_x/\sigma_z \geq 200$. This figure does not depend on the forcing amplitude u_0.

rameterizing a complicated wave dissipation event by a body forcing with averaged temporal and spatial distributions would underestimate, potentially severely, the amplitudes of the higher-frequency, secondary gravity waves. Because it is the higher-frequency waves that are expected to most easily propagate to greater altitudes, it is important to include spatial and temporal variability into any parameterization scheme to be used in global-scale models. Our results imply both an important role of spatially and temporally localized body forces in the radiation of gravity waves and a potential to quantify the role of such radiation in the atmosphere.

Finally, the mean responses are not confined to the source region; in general, significant spatial broadening of the mean responses occurs in one direction. By ''broadening'' we mean that a spatial extent of the mean response is larger (potentially much larger) than the spatial extent of the source in the same direction. If a source has a high characteristic frequency, the mean responses are generally broadened meridionally and zonally if $\sigma_y \ll \sigma_x$ and $\sigma_x \ll \sigma_y$, respectively. If a source has a low characteristic frequency, the mean responses are generally broadened vertically. The amount of broadening that occurs depends sensitively on the characteristic spatial scales of the source but not on the spatial extent of the source in the direction of the broadening. Equation (5.3) is a handy formula relating these quantities. In addition, the mean zonal (meridional) wind just outside the source region in the $\pm y$ ($\pm x$) direction is commonly in the opposing direction to the direction of the zonal (meridional) body force (i.e., ''countersigned'' winds).

In cases where the body force geometry is determined by source conditions, that is, convection or orography, with high-frequency motions occupying a volume of tens to hundreds of kilometers horizontally and dissipating over tens of kilometers vertically, the momentum source is deep and will broaden along the direction of minimum horizontal extent. For example, a zonally confined wave field excited by extended north–south mountains would excite a circulation that would broaden zonally. Alternatively, tidal filtering of a localized, convectively generated gravity wave field might resemble a dipole-in-z source with σ_x, $\sigma_y \sim$ a few hundred kilometers and a vertical scale of $\sigma_z \sim 10$ km. The mean response generated from this source may not broaden very much because the horizontal extents of the source are similar.

There are a number of important implications of these findings for spatially and temporally varying body forcings in the atmosphere. First, these results do not impact the inference of mean forcing by mean gravity wave momentum flux divergence. Thus, prescription of such forcing in large-scale models will yield the mean response accompanying a statistical forcing having the same mean values. Second, the radiation of gravity waves, especially for 3D forcings that are spatially localized with $\sigma_x \lesssim \sigma_y$) and temporally confined (i.e., $\hat{a} \gtrsim \omega_c$), is very efficient and occurs on spatial scales comparable to or larger than the forcing scales. For scales representative of expected forcing by convectively or orographically generated gravity waves (σ_x and $\sigma_y \sim$ a few hundred kilometers and $\sigma_z \sim 10$ km), the wave scales and frequencies are sufficiently large to imply that they may propagate largely unimpeded to much greater altitudes. This is potentially a very significant result, as there has been little attention to date devoted to the effects that such fast, large-scale motions may have in forcing the mesosphere and lower thermosphere. Finally, these results may have interesting implications for the parameterization of gravity wave effects and transports given that at least at higher altitudes, an increasing fraction of the effects may be due to radiated waves rather than waves that have propagated from sources at lower altitudes in a deterministic manner.

Acknowledgments. S. L. Vadas and D. C. Fritts were supported by NASA Contract S-46331-G, NSF Grants ATM-9618004 and ATM-9708633, and AFOSR Contract F49620-98-C-0029. The authors are grateful to M. J. Alexander for her useful, interesting discussions and careful reading of this paper. The authors would also like to thank S. C. Arendt for useful discussions and our anonymous referees for their helpful comments.

APPENDIX A

Validity of Linear Boussinesq Theory for Zonal Forcings

The linear Boussinesq zonal-forcing solutions derived in this paper are only valid for forcing amplitudes that are ''small.'' The flow Mach number must be less than 1, or $u_0 < 2.2HN \simeq 300$ m s^{-1}. In addition, nonlinear wave–wave and wave–mean interactions must be small; we estimate that $|(\mathbf{v}\cdot\nabla)\mathbf{v}| < |\partial\mathbf{v}/\partial t|$, and $|(\mathbf{v}\cdot\nabla)\Theta| < |\partial\Theta/\partial t|$. We estimate the derivatives of the mean responses using the results of section 5b (e.g., $|\partial\overline{u}/\partial y| \simeq \overline{u}/2\Delta_y$), and calculate the derivatives of the gravity wave responses using the fast-forcing solution frequencies and wavelengths determined in section 4a (e.g., $|\partial u_{GW}/\partial y| \simeq u_{GW}2\pi/9\sigma_y$). Following section 5e, we crudely estimate the maximal mean and gravity wave amplitudes by calculating the spectral amplitudes of the solutions at their characteristic wavenumbers. In order that nonlinear interactions are small 1) $u_0 < 2f\sigma_y$ for zonally symmetric forces and 2) $u_0 < N\sigma_z$ for meridionally symmetric forces with negligible rotation. Slower forcings would result in larger allowable forcing amplitudes. These estimates are conservative even for impulsive forcings because the average mean and gravity wave amplitudes are less than the maximal values.[A1]

[A1] Vadas et al. 2001 (unpublished manuscript) contains a better calculation of the validity of the linear equations.

APPENDIX B

3D Initial Value and Impulsive Forcing Spectral Solutions

We obtain the spectral vertical velocity by calculating the functional form of the Laplace inversion integral of Eq. (3.2) when $A_F = B_F = 0$. The other variables are determined similarly. The 3D initial value and impulsive body forced spectral solutions are then

$$\tilde{w}(t) = A_I \cos\omega t + \frac{B_I}{\omega}\sin\omega t, \tag{B.1}$$

$$\tilde{\Theta}(t) = \tilde{\Theta}(0) - N^2\left[\frac{A_I}{\omega}\sin\omega t - \frac{B_I}{\omega^2}(\cos\omega t - 1)\right], \tag{B.2}$$

$$\tilde{P}(t) = -\frac{i}{m}\left[\left(1 - \frac{N^2}{\omega^2}\right)(-A_I\omega\sin\omega t + B_I\cos\omega t) - \tilde{\Theta}(0) + \frac{B_I N^2}{\omega^2}\right], \tag{B.3}$$

$$\tilde{v}(t) = -\frac{m}{k_H^2}\left[\left(lA_I + fk\frac{B_I}{\omega^2}\right)\cos\omega t + \frac{lB_I - fkA_I}{\omega}\sin\omega t\right] + \frac{k}{k_H^2}\left[fm\frac{B_I}{\omega^2} + k\tilde{v}(0) - l\tilde{u}(0)\right], \tag{B.4}$$

$$\tilde{u}(t) = -\frac{m}{k_H^2}\left[\left(kA_I - fl\frac{B_I}{\omega^2}\right)\cos\omega t + \frac{kB_I + flA_I}{\omega}\sin\omega t\right] - \frac{l}{k_H^2}\left[fm\frac{B_I}{\omega^2} + k\tilde{v}(0) - l\tilde{u}(0)\right], \tag{B.5}$$

where

$$A_I = \tilde{w}(0),$$

$$B_I = \frac{1}{\mathbf{k}^2}[k_H^2\tilde{\Theta}(0) + fm(l\tilde{u}(0) - k\tilde{v}(0))]. \tag{B.6}$$

If $m = 0$, then $\tilde{w}(t) = \tilde{w}(0)\cos Nt + (\tilde{\Theta}(0)/N)\sin Nt$, $\tilde{\Theta}(t) = \tilde{\Theta}(0)\cos Nt - N\tilde{w}(0)\sin Nt$, $\tilde{u}(t) = \tilde{u}(0)$, $\tilde{v}(t) = \tilde{v}(0)$, and $\tilde{P}(t) = -if\tilde{u}(0)/l$. If $k_H^2 = 0$, then $\tilde{u}(t) = \tilde{u}(0)\cos ft + \tilde{v}(0)\sin ft$ and $\tilde{v}(t) = \tilde{v}(0)\cos ft - \tilde{u}(0)\sin ft$. If $\mathbf{k}^2 = 0$, then $\tilde{P}(t) = 0$.

APPENDIX C

Special Case of the Forced Interval Solutions

When $m = 0$, $\tilde{w}(t)$ and $\tilde{\Theta}(t)$ are the solutions in section 3b with $\omega = N$. When $k_H^2 = 0$,

$$\tilde{u}(t) = \frac{1}{f\sigma(\hat{a}^2 - f^2)} \times \{\alpha(\tilde{F}_x\hat{a}[\hat{a}\sin ft - f\sin\hat{a}t] + \tilde{F}_y[\hat{a}^2(1-\cos ft) - f^2(1-\cos\hat{a}t)]) + \beta\hat{a}^2(\tilde{F}_x\mathcal{S} - \tilde{F}_y\mathcal{C})\}, \tag{C.1}$$

$$\tilde{v}(t) = \frac{1}{f\sigma(\hat{a}^2 - f^2)} \times \{\alpha(\tilde{F}_y\hat{a}[\hat{a}\sin ft - f\sin\hat{a}t] - \tilde{F}_x[\hat{a}^2(1-\cos ft) - f^2(1-\cos\hat{a}t)]) + \beta\hat{a}^2(\tilde{F}_x\mathcal{C} + \tilde{F}_y\mathcal{S})\}, \tag{C.2}$$

regardless of m, where $\mathcal{S}$ and $\mathcal{C}$ are evaluated at $\omega = f$, $\alpha = 1$ and $\beta = 0$ when $t \le \sigma$, and $\alpha = 0$ and $\beta = 1$ when $t \ge \sigma$. When $k = l = m = 0$, then $\tilde{P}(t) = 0$.

APPENDIX D

Newtonian Solution for a Ball-and-Block System

Here, we derive the equations of motion governing the ball-and-block Newtonian system described in section 3g. The system kinetic and potential energies are $M\dot{X}^2/2 + m(\dot{x}_{lab}^2 + \dot{z}_{lab}^2)/2$ and $mgl(1 - \cos\xi) - \int F_{block}\,dX$, respectively, where the dot denotes $\dot{} = \partial/\partial t$ and where (x_{lab}, z_{lab}) is the ball's location in the lab frame. Using the small-angle approximation (i.e., $|\xi| \ll 1$), the Lagrangian is

$$L = \frac{1}{2}M\dot{X}^2 + \frac{1}{2}m(l^2\dot{\xi}^2 - 2l\dot{\xi}\dot{X} + \dot{X}^2) - \frac{1}{2}mgl\xi^2 + \int F_{block}\,dX. \tag{D.1}$$

The equations of motion, $\partial L/\partial q_i - d/dt(\partial L/\partial\dot{q}_i) = 0$, where $q_i = X$ and ξ, are

$$ml\ddot{\xi} = m\ddot{X} - mg\xi, \qquad M\ddot{X} = F_{block} - mg\xi. \tag{D.2}$$

Defining the natural pendulum frequency to be $\omega = ((g/l)(1 + m/M))^{1/2}$, the solution is[D1]

$$\xi(t \le \sigma) = \frac{V_0}{g\sigma}\left[1 - \frac{\hat{a}^2}{\hat{a}^2 - \omega^2}\cos\omega t + \frac{\omega^2}{\hat{a}^2 - \omega^2}\cos\hat{a}t\right], \tag{D.3}$$

$$\xi(t \ge \sigma) = \frac{V_0\hat{a}^2}{g\sigma(\hat{a}^2 - \omega^2)} \times [\sin\omega\sigma\sin\omega t - (1 - \cos\omega\sigma)\cos\omega t]. \tag{D.4}$$

The block's postforcing, horizontal velocity ($U = \dot{X}$) oscillates in time about the mean V_0:

$$U(t \ge \sigma) = V_0\left\{1 + \frac{m\hat{a}^2}{M\omega\sigma(\hat{a}^2 - \omega^2)} \times [(1 - \cos\omega\sigma)\sin\omega t + \sin\omega\sigma\cos\omega t]\right\}. \tag{D.5}$$

[D1] It can be shown that the ball-and-block solution is well defined when $\hat{a} = \omega$.

The oscillatory motion is multiplied by $\hat{a}^2/\omega\sigma(\hat{a}^2 - \omega^2)$, which is the same factor as for the gravity waves [see Eqs. (3.13)–(3.17)]. The postforcing total system energy is the work done:

$$E(t \geq \sigma) = \int F_{\text{block}}\, dX = \int_0^{\sigma} F_{\text{block}} U\, dt$$

$$= \frac{1}{2}(m + M)V_0^2\left[1 + \frac{4m}{M}\frac{\hat{a}^4 \sin^2(\omega\sigma/2)}{(\omega\sigma)^2(\hat{a}^2 - \omega^2)^2}\right]. \quad \text{(D.6)}$$

The first and second terms in square brackets are due to the mean and oscillatory responses, respectively. The multiplying factor for the energy due to oscillatory motions, $4\hat{a}^4 \sin^2(\omega\sigma/2)/(\omega\sigma)^2(\hat{a}^2 - \omega^2)^2$, is the same as for the gravity wave spectral energy density [see Eq. (3.27)]. Therefore, the oscillatory amplitudes and energy are small and large when $\omega \gg \hat{a}$ and $\omega\sigma \ll 1$, respectively. In the fast-forcing limit, the fraction of energy in oscillatory motions is $(1 + M/m)^{-1}$ from Eq. (D.6). Comparing this with Eq. (5.10), we identify m/M with $(\sigma_y/R)^2 + (\sigma_y/\sigma_x)^2$ for atmospheric zonal forcings.

REFERENCES

Abramowitz, M., and I. A. Stegun, 1972: *Handbook of Mathematical Functions.* Dover Publications, 1045 pp.

Alexander, M. J., 1996: A simulated spectrum of convectively generated gravity waves: Propagation from the tropopause to the mesopause and effects on the middle atmosphere. *J. Geophys. Res.,* **101,** 1571–1588.

——, 1997: A model of non-stationary gravity waves in the stratosphere and comparison to observations, *Gravity Wave Processes and their Parameterization in Global Climate Models,* K. Hamilton, Ed., NATO ASI Series, Vol. 50, Springer-Verlag, 153–168.

——, and K. H. Rosenlof, 1996: Nonstationary gravity wave forcing of the stratospheric zonal mean wind. *J. Geophys. Res.,* **101,** 23 465–23 474.

——, J. R. Holton, and D. R. Durran, 1995: The gravity wave response above deep convection in a squall line simulation. *J. Atmos. Sci.,* **52,** 2212–2226.

Andreassen, Ø., P. Ø. Hvidsten, D. C. Fritts, and S. Arendt, 1998: Vorticity dynamics in a breaking internal gravity wave. Part 1. Initial instability evolution. *J. Fluid Mech.,* **367,** 27–46.

Andrews, D. G., J. R. Holton, and C. B. Leovy, 1987: *Middle Atmosphere Dynamics.* Academic Press, 489 pp.

Blumen, W., 1972: Geostrophic adjustment. *Rev. Geophys. Space Phys.,* **10,** 485–528.

Bühler, O., M. E. McIntyre, and J. F. Scinocca, 1999: On shear-generated gravity waves that reach the mesosphere. Part I: Wave generation. *J. Atmos. Sci.,* **56,** 3749–3763.

Dickinson, R. E., 1969: Propagators of atmospheric motions. 1. Excitation by point impulses. *Rev. Geophys.,* **7,** 483–538.

Dunkerton, T. J., 1982: Stochastic parameterization of gravity wave stresses. *J. Atmos. Sci.,* **39,** 1711–1725.

——, 1989: Body force circulations in a compressible atmosphere: Key concepts. *Pure Appl. Geophys.,* **130,** 243–262.

Durran, D. R., and J. B. Klemp, 1987: Another look at downslope winds. Part II: Nonlinear amplification beneath wave overturning layers. *J. Atmos. Sci.,* **44,** 3402–3412.

Fovell, R., D. Durran, and J. R. Holton, 1992: Numerical simulation of convectively generated gravity waves. *J. Atmos. Sci.,* **49,** 1427–1442.

Franke, P. M., and W. A. Robinson, 1999: Nonlinear behavior in the propagation of atmospheric gravity waves. *J. Atmos. Sci.,* **56,** 3010–3027.

Fritts, D. C., and R. A. Vincent, 1987: Mesospheric momentum flux studies at Adelaide, Australia: Observations and a gravity wave/tidal interaction model. *J. Atmos. Sci.,* **44,** 605–619.

——, and Z. Luo, 1992: Gravity wave excitation by geostrophic adjustment of the jet stream. Part 1: Two-dimensional forcing. *J. Atmos. Sci.,* **49,** 681–697.

——, and G. D. Nastrom, 1992: Sources of mesoscale variability of gravity waves. Part II: Frontal, convective, and jet stream excitation. *J. Atmos. Sci.,* **49,** 111–127.

——, and T. E. VanZandt, 1993: Spectral estimates of gravity wave energy and momentum fluxes. Part I: Energy dissipation, acceleration, and constraints. *J. Atmos. Sci.,* **50,** 3685–3694.

——, and Z. Luo, 1995: Dynamical and radiative forcing of the summer mesopause circulation and thermal structure. 1. Mean Solstice conditions. *J. Geophys. Res.,* **100,** 3119–3128.

Gall, R. L., R. T. Williams, and T. L. Clark, 1988: Gravity waves generated during frontogenesis. *J. Atmos. Sci.,* **45,** 2204–2219.

Garcia, R. R., 1987: On the mean meridional circulation of the middle atmosphere. *J. Atmos. Sci.,* **44,** 3599–3609.

——, 1989: Dynamics, radiation, and photochemistry in the mesosphere: Implications for the formation of noctilucent clouds. *J. Geophys. Res.,* **94,** 14 605–14 615.

——, and B. A. Boville, 1994: ''Downward control'' of the mean meridional circulation and temperature distribution of the polar winter stratosphere. *J. Atmos. Sci.,* **51,** 2238–2245.

Gill, A., 1982: *Atmosphere–Ocean dynamics.* Academic Press, 662 pp.

Haynes, P. H., C. J. Marks, M. E. McIntyre, T. G. Shephard, and K. P. Shine, 1991: On the ''Downward Control'' of extratropical diabatic circulations by eddy-induced mean zonal forces. *J. Atmos. Sci.,* **48,** 657–678.

Hitchman, M. H., J. C. Gille, C. D. Rodgers, and G. Brasseur, 1989: The separated polar winter stratopause: A gravity wave driven climatological feature. *J. Atmos. Sci.,* **46,** 410–422.

Holton, J. R., 1982: The role of gravity wave-induced drag and diffusion in the momentum budget of the mesosphere. *J. Atmos. Sci.,* **39,** 791–799.

——, 1983: The influence of gravity wave breaking on the general circulation of the middle atmosphere. *J. Atmos. Sci.,* **40,** 2497–2507.

——, and M. J. Alexander, 1999: Gravity waves in the mesosphere generated by tropospheric convection. *Tellus,* **51A-B,** 45–58.

Kelley, M. C., 1997: In situ ionospheric observations of severe weather-related gravity waves and associated small-scale plasma structure. *J. Geophys. Res.,* **102,** 329–335.

LeLong, M.-P., and T. J. Dunkerton, 1998: Inertia–gravity wave breaking in three dimensions. Part I: Convectively stable waves. *J. Atmos. Sci.,* **55,** 2473–2488.

Luo, Z., and D. C. Fritts, 1993: Gravity wave excitation by geostrophic adjustment of the jet stream. Part II: Three-dimensional forcing. *J. Atmos. Sci.,* **50,** 104–115.

——, ——, R. W. Portmann, and G. E. Thomas, 1995: Dynamical and radiative forcing of the summer mesopause circulation and thermal structure. 2. Seasonal variations. *J. Geophys. Res.,* **100,** 3129–3137.

McFarlane, N. A., 1987: The effect of orographically excited gravity wave drag on the general circulation of the lower stratosphere and troposphere. *J. Atmos. Sci.,* **44,** 1775–1800.

McIntyre, M. E., 1989: On dynamics and transport near the polar mesopause in summer. *J. Geophys. Res.,* **94,** 14 617–14 628.

Nastrom, G. D., and D. C. Fritts, 1992: Sources of mesoscale variability of gravity waves. Part I: Topographic excitation. *J. Atmos. Sci.,* **49,** 101–110.

——, B. B. Balsley, and D. A. Carter, 1982: Mean meridional winds

in the mid- and high-latitude summer mesosphere. *Geophys. Res. Lett.*, **9,** 139–142.

Palmer, T. N., G. J. Shutts, and R. Swinbank, 1986: Alleviation of a systematic westerly bias in general circulation and numerical weather prediction models through an orographic gravity wave drag parameterization. *Quart. J. Roy. Meteor. Soc.*, **112,** 1001–1040.

Rossby, C.-G., 1936: Dynamics of steady ocean currents in the light of experimental fluid mechanics. *Pap. Phys. Oceanogr. Meteor.*, **5**.

——, 1937: On the mutual adjustment of pressure and velocity distributions in certain simple current systems, 1. *J. Mar. Res.*, **1,** 15–28.

——, 1938: On the mutual adjustment of pressure and velocity distributions in certain simple current systems, 2. *J. Mar. Res.*, **1,** 239–263.

Salby, M. L., and R. R. Garcia, 1987: Transient response to localized episodic heating in the tropics. Part I: Excitation and short-time near-field behavior. *J. Atmos. Sci.*, **44,** 458–498.

Satomura, T., and K. Sato, 1999: Secondary generation of gravity waves associated with the breaking of mountain waves. *J. Atmos. Sci.*, **56,** 3847–3858.

Taylor, M. J., and M. A. Hapgood, 1988: Identification of a thunderstorm as a source of short period gravity waves in the upper atmospheric nightglow emissions. *Planet. Space Sci.*, **36,** 975–985.

VanZandt, T. E., and D. C. Fritts, 1989: A theory of enhanced saturation of the gravity wave spectrum due to increases in atmospheric stability. *Pure Appl. Geophys.*, **130,** 399–420.

Walterscheid, R. L., and D. J. Boucher Jr., 1984: A simple model of the transient response of the thermosphere to impulsive forcing. *J. Atmos. Sci.*, **41,** 1062–1072.

Zhu, X., and J. R. Holton, 1987: Mean fields induced by local gravity-wave forcing in the middle atmosphere. *J. Atmos. Sci.*, **44,** 620–630.